Draft version January 13, 2022
Preprint typeset using LaTeX style emulateapj v. 12/16/11

GIANT PRIMEVAL MAGNETIC DIPOLES

Christopher Thompson
Canadian Institute for Theoretical Astrophysics, 60 St. George St., Toronto, ON M5S 3H8, Canada.
Draft version January 13, 2022

ABSTRACT

Macroscopic magnetic dipoles are considered as cosmic dark matter. Permanent magnetism in relativistic field structures can involve some form of superconductivity, one example being current-carrying string loops ('springs') with vanishing net tension. We derive the cross section for free classical dipoles to collide, finding it depends weakly on orientation when mutual precession is rapid. The collision rate of 'spring' loops with tension $\mathcal{T} \sim 10^{-8} c^4/G$ in galactic halos approaches the measured rate of fast radio bursts (FRBs) if the loops comprise most of the dark matter. A large superconducting dipole (LSD) with mass $\sim 10^{20}$ g and size ~ 1 mm will form a ~ 100 km magnetosphere moving through interstellar plasma. Although hydromagnetic drag is generally weak, it is strong enough to capture some LSDs into long-lived rings orbiting supermassive black holes (SMBHs) that form by the direct collapse of massive gas clouds. Repeated collisions near young SMBHs could dominate the global collision rate, thereby broadening the dipole mass spectrum. Colliding LSDs produce tiny, hot electromagnetic explosions. The accompanying paper shows that these explosions couple effectively to propagating low-frequency electromagnetic modes, with output peaking at 0.01-1 THz. We describe several constraints on, and predictions of, LSDs as cosmic dark matter. The shock formed by an infalling LSD triggers self-sustained thermonuclear burning in a C/O (ONeMg) white dwarf (WD) of mass $\gtrsim 1\,M_\odot$ ($1.3\,M_\odot$). The spark is generally located well off the center of the WD. The rate of LSD-induced explosions matches the observed rate of Type Ia supernovae.

1. INTRODUCTION

We consider macroscopic magnets as a component of the cosmic dark matter, showing that the hypothesis has a number of interesting observational consequences. The underlying theoretical motivation, although slender, goes back to the demonstration that cosmic strings may carry substantial electric currents (Witten 1985). In some circumstances the magnetic field winding around the string grows strong enough to compensate the relativistic string tension, in which case macroscopic static loops of the string would survive indefinitely as a form of kinematically cold dark matter (Ostriker et al. 1986; Copeland et al. 1987; Haws et al. 1988; Davis & Shellard 1989). But the possibility of relativistic field structures carrying a magnetic dipole moment is a more general one.

Our interest here is in the interactions between these large superconducting dipoles (LSDs) which, although individually rare, can collectively be quite frequent. Direct collisions are a source of intense, but narrow, electromagnetic pulses, details of which are examined in the companion paper (Thompson 2017, hereafter Paper I). In fact, the motivation for this investigation was provided by the discovery of rapid and intense radio bursts (FRBs; Lorimer et al. 2007; Thornton et al. 2013) occurring at a rate of about 3×10^3 per day above a fluence threshold of $\sim 5 \times 10^{-17}$ erg cm^{-2} (Crawford et al. 2016), or $1-3\times10^4$ per day as inferred from the one demonstrated repeating source (Scholz et al. 2016). The pulses are highly dispersed, suggesting a cosmological origin, which has recently been confirmed indirectly by a measurement of Faraday rotation (Ravi et al. 2016), and directly by localization (Chatterjee et al. 2017; Marcote et al. 2017; Tendulkar et al. 2017). Then the energy emitted in the GHz band reaches at least 10^{39} erg in some cases (unless the emission is highly beamed: Luan & Goldreich 2014; Katz 2016).

We show here that two channels are available for LSD collisions. Very rarely LSDs orbiting in galactic halos will collide with each other. A small subset of LSDs can also be captured gravitationally by supermassive black holes (SMBHs) if the holes form by direct collapse of dense gas clouds. The collision rate through the first channel approaches the (still roughly) measured FRB rate if the LSDs i) comprise a significant fraction of the cosmic dark matter; ii) have a large enough mass to power a FRB, after allowing for a $\sim$ 1-10% efficiency of GHz emission (Paper I); and iii) have magnetic fields not far below the electroweak scale (10^{24} G). In the 'spring' model conditions ii) and iii) implyd a string tension $\mathcal{T} \sim 10^{-8} c^4/G$.

Each LSD orbiting through a galaxy forms a small magnetosphere and experiences very weak drag off the surrounding plasma. However, the drag effect is more significant for the LSDs that are adiabatically compressed close to a newly formed SMBH following its collapse. These dipoles settle gradually toward the innermost stable circular orbit (ISCO), just outside of which the drag force vanishes. We show that collisions significantly broaden their mass distribution, allowing for a range of radio pulse energies starting from a peaked primordial mass distribution. In this dense environment, a large fraction of the dipoles are removed by collisions. The companion paper also shows that a GHz pulse can escape this environment if the black hole has entered a phase of weak and radiatively inefficient accretion.

A significant contribution of LSDs to the dark matter just above the mass range considered here ($\sim 10^{20}$ g) is strongly constrained by sub-pixel microlensing (Niikura et al. 2017). Destructive collisions with white

dwarfs (WDs) have also been considered as a limitation on the abundance of primordial black holes around this mass (Capela et al. 2013; Graham et al. 2015). A LSD that is gravitationally deflected into a WD will produce a similarly localized heating. We calculate the critical WD mass (central density) above which this heating triggers self-sustained thermonuclear burning, which turns out to depend on the WD composition, and consider whether the heated zone is large enough to drive a direct detonation. The calculated rate of thermonuclear explosions is close to the observed Type Ia rate, and there is an interesting prediction of a depletion of old and massive WDs in the Solar neighborhood.

The existence of the LSDs considered here does not strictly imply the presence of a network of horizon-crossing cosmic strings or oscillating string loops. Nonetheless existing bounds on local string networks from pulsar timing (e.g. Lentati et al. 2015) are consistent with the range of tensions considered here. Strong gravitational lensing by the long string (Kaiser & Stebbins 1984) would be restricted to subarcsecond angular scales.

The web of physical processes described here and in Paper I is applied to the repeating FRB 121102. Gravitational lensing by a $\sim 10^6\, M_\odot$ SMBH naturally generates a minimum time delay of ~ 30 s. We show that reflection of a strong electromagnetic pulse by dense plasma clouds is restricted to larger distances from the black hole, corresponding to time delays of hundreds of seconds. Both of these timescales are present in the observed activity of FRB 121102 (Spitler et al. 2016; Scholz et al. 2016). The pulses emerging from close to a SMBH are expected to show strong Faraday rotation, or even be depolarized at finite bandwidth.

A key prediction of the model is 0.01-1 THz pulses even brighter and narrower than FRBs (Paper I). High-frequency measurements directly probe the underyling field structure if FRBs are powered by 'tiny' electromagnetic explosions. High-frequency pulses can escape from relatively dense plasma clouds around SMBHs, and are a possible source of 'noise' in CMB experiments. Detecting them would discriminate between emission from plasma structures of a size larger than a radio wavelength λ, versus relativistic field structures smaller than λ. One expects the emission to be weaker at longer wavelengths if the emitting plasma is comparable in size to a neutron star.

The redshift distribution of electromagnetic pulses from colliding LSDs depends on whether the collision rate is dominated by compact rings orbiting SMBHs, or instead by rare collision events distributed throughout galactic halos. In the first case, the FRB emission is weighted toward higher redshifts, closer to the epoch of collapse of the first SMBHs. In addition, only SMBHs which form directly from gas collapse and do not merge with other SMBHs are potential emission sites of FRBs. We show that the LSD ring around a SMBH does survive repeat injections of very dense plasma from the tidal disruption of stars.

Finally, the nearest LSD is predicted to lie about 20 AU from the Sun, and move with extreme proper motion with a residency time of ~ 0.3 yr. Scaling down from planetary magnetospheres suggest that the ~ 100 km zone around the nearest LSD is a possible μJy source of coherent radio emission.

The plan of this paper is as follows. The cross section for the collision of free classical magnetic dipoles is presented in Section 2, with further details in the Appendix. The interaction of a moving LSD with ambient plasma is described in Section 3, including trapping near SMBHs. The rate of collisions between LSDs bound in galactic halos is calculated in Section 4. The identification of LSDs with GUT-scale superconducting 'spring' loops is considered in Section 5. The collisional evolution of the dipole number, mass spectrum, and radiation energy spectrum of a LSD ring near the ISCO of a SMBH is calculated in Section 6. Details of the interaction with realistic model WDs can be found in Section 7. The concluding Section 8 describes various tests, observational consequences, and predictions of LSD dark matter and LSD collisions as the mechanism of FRBs.

2. COLLISION CROSS SECTION OF CLASSICAL MAGNETIC DIPOLES (IN VACUUM)

Here we calculate the cross section for two classical magnetic dipoles to collide. The dipoles are otherwise unbound and assumed to propagate in a vacuum. When the magnetic field contributes a significant part of the inertia of each dipole, ambient plasma screens the magnetic field only on much larger scales than the collision impact parameter.

The relation between magnetic dipole moment μ and rest mass $\mathcal{M}$ is normalized to

$$f_{\rm em}\mathcal{M}c^2 = \mu^2\mathcal{R}^{-3}, \tag{1}$$

where $\mathcal{R}$ is a characteristic radius. Setting the coefficient $f_{\rm em}$ on the left-hand side to unity gives the electromagnetic inertia of a uniformly magnetized sphere of radius $\mathcal{R}$, in which case the relation between mass and radius is[1] $\mathcal{M} \sim 3\times 10^{19}\, B_{22}^2\mathcal{R}_{-1}^3$ g. Additional (e.g. toroidal or scalar) field components are needed to stabilize the dipole, and so we expect $f_{\rm em} \lesssim 1$. A concrete example is given in Section 5.

Two colliding dipoles will merge if the $-\boldsymbol{\mu}\cdot\mathbf{B}$ energy grows in magnitude above their initial kinetic energy. Because the dipole-dipole interaction scales as r^{-3}, there is no centrifugal barrier to a direct collision. Then a first estimate of the collision impact parameter of two identical dipoles is

$$b_{\rm col} \sim R_{\rm col} \equiv \left(\frac{\mu^2}{\mathcal{M}v^2}\right)^{1/3} = f_{\rm em}^{1/3}\left(\frac{v}{c}\right)^{-2/3}\mathcal{R} = 10\, f_{\rm em}^{1/3}\, v_{7.5}^{-2/3}\mathcal{R}_{-1} \quad \text{cm}. \tag{2}$$

Here v is the velocity at infinity of each dipole. This cross section depends on the dipole size, but not individually on μ and $\mathcal{M}$.

The initial orientation of the dipoles does not matter as long as each dipole precesses rapidly in the magnetic field of the other. The precession frequency of one dipole in the magnetic field of a second is

$$\omega_g = \left(\frac{|\boldsymbol{\mu}_1\times\mathbf{B}_2(\mathbf{r}_{12})|}{\mathcal{I}_1}\right)^{1/2}, \tag{3}$$

[1] Throughout this paper we use the shorthand $X = X_n \times 10^n$, where quantity X is expressed in c.g.s. units.

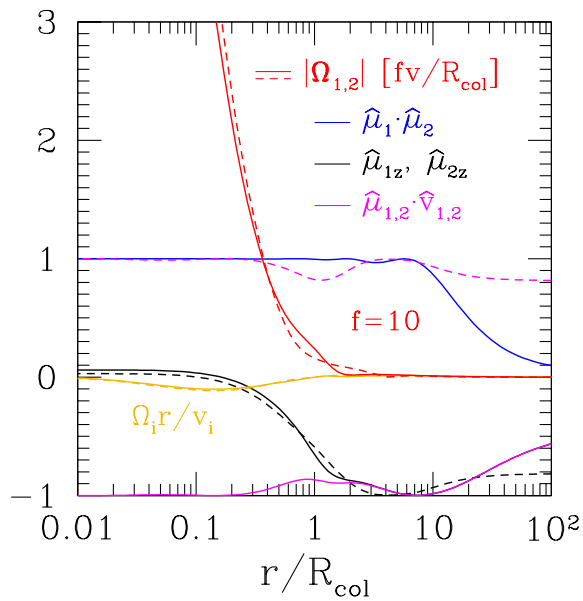

FIG. 1.— Two classical magnetic dipoles collide along the z-axis with vanishing initial rotation, and fastness parameter (5) $f = 10$. Black lines: projection of unit magnetic moment onto the collision axis. Blue line: relative orientation of the two moments. Magenta lines: projection $\hat{\mu}_i \cdot \hat{v}_i$ of magnetic moment $i = 1, 2$ on velocity, which is nearly radial inside the collision radius $R_{\rm col}$. Red lines: dipole spin vectors in units of $fv/R_{\rm col}$, where v is velocity of each dipole at infinity. Gold lines: spin frequency multiplied by the collision time.

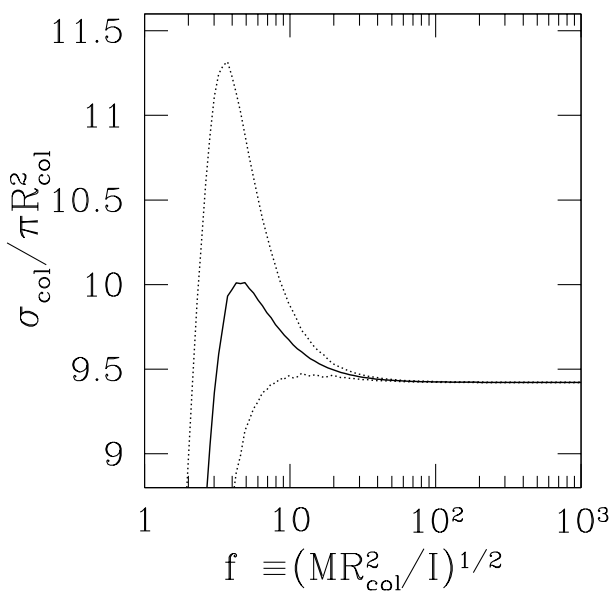

FIG. 2.— Solid line: mean cross section for the collision of two classical and non-relativistic dipoles in vacuum, as a function of the fastness parameter $f \equiv (\mathcal{M}R^2_{\rm col}/I)^{1/2}$. Dotted curves show the variance in the result for randomly oriented magnetic moments, with vanishing initial spins.

where $\mathbf{r}_{12} \equiv \mathbf{r}_1 - \mathbf{r}_2$ is the separation. This works out to

$$\frac{\omega_g(R_{\rm col})}{v/R_{\rm col}} \sim f(\mu, v) \equiv \left(\frac{\mathcal{M}R^2_{\rm col}}{\mathcal{I}}\right)^{1/2} \sim \frac{R_{\rm col}}{\mathcal{R}} \qquad (4)$$

at the capture impact parameter $r_{12} \sim R_{\rm col}$. The fastness parameter f can be written as

$$f(\mu, v) = f_{\rm em}^{1/3} \left(\frac{v}{c}\right)^{-2/3} \left(\frac{\mathcal{I}}{\mathcal{M}\mathcal{R}^2}\right)^{-1/2} = 100\, f_{\rm em}^{1/3} v_{7.5}^{-2/3} \left(\frac{\mathcal{I}}{\mathcal{M}\mathcal{R}^2}\right)^{-1/2}. \qquad (5)$$

Here $\mathcal{I}$ is the moment of inertia of a dipole, whose rotational degrees of freedom are reduced to those of a sphere.

In the regime of rapid precession ($f \gg 1$), two dipoles reaching a separation $\lesssim R_{\rm col}$ quickly rotate into a configuration with each magnetic moment nearly aligned parallel (anti-parallel) to its radial velocity, $\hat{v} \cdot \hat{\mu} = \pm 1$, and $\hat{\mu}_1 \cdot \hat{\mu}_2 = 1$ (Figure 1). This generates an attractive force and minimizes the torque, the precession rate, and the interaction energy

$$\mathcal{E}_{12} = \frac{\boldsymbol{\mu}_1 \cdot \boldsymbol{\mu}_2 - 3(\boldsymbol{\mu}_1 \cdot \hat{r}_{12})(\boldsymbol{\mu}_2 \cdot \hat{r}_{12})}{r_{12}^3} = -\frac{2\boldsymbol{\mu}_1 \cdot \boldsymbol{\mu}_2}{r_{12}^3}. \qquad (6)$$

The generalization to dipoles with unequal magnetic moments and masses is straightforward. The collision radius is now defined as

$$R_{\rm col} \equiv \left[\frac{2\mu_1\mu_2}{\mathcal{M}_r(\Delta v)^2}\right]^{1/3}. \qquad (7)$$

Here $\mathcal{M}_r = \mathcal{M}_1\mathcal{M}_2/(\mathcal{M}_1 + \mathcal{M}_2)$ is the reduced mass, and Δv is the relative velocity at infinity. This expression matches (2) when $\mu_1 = \mu_2$ and $\mathcal{M}_1 = \mathcal{M}_2$, taking into account $\Delta v \to 2v$. Complications with differing moments of inertia can be neglected when $f \gg 1$.

To evaluate the dispersion in capture cross section at finite f, we calculate numerically a large set of trajectories with random orientations of $\boldsymbol{\mu}_i$ ($i = 1, 2$) with respect to the collision axis and vanishing initial spins. Figure 2 shows the result. The cross section at infinite f is

$$b_{\rm col}(f = \infty) = 1.732\, R_{\rm col}; \quad \sigma_{\rm col}(f = \infty) = 9.42\, R^2_{\rm col}. \qquad (8)$$

The variance in $\sigma_{\rm col}$ decreases to a few percent at $f = 10$, and asymptotes to zero as $f \to \infty$. Notice that the collision rate depends weakly on the velocity dispersion of the dipoles, e.g. on the depth of the Galactic potential, since $\sigma_{\rm col} v \propto v^{-1/3}$. Further details of the calculation, including a demonstration that the result depends only on $R_{\rm col}$ as defined in Equation (7) when $f \gg 1$, can be found in the Appendix.

2.1. *Gravitational Effects*

The gravitational interaction between two dipoles must be taken into account when they move sufficiently slowly, and the collision impact parameter $b_{\rm col}$ becomes large enough that $G\mathcal{M}^2/b_{\rm col} \gtrsim \mu^2/b^3_{\rm col}$. The critical speed above which the magnetic interaction dominates is

$$\frac{v}{c} \simeq 2.3\, f_{\rm em}^{-1/4} \left(\frac{G\mathcal{M}}{\mathcal{R}c^2}\right)^{3/4} = 1.0 \times 10^{-5} f_{\rm em}^{-1/4} \mathcal{M}_{20}^{3/4} \mathcal{R}_{-1}^{-3/4} \qquad (9)$$

in the center of mass frame.

2.2. *Post-Collision Relaxation*

As the two dipoles approach each other, conservation of $\mathbf{\Omega}_i \cdot \boldsymbol{\mu}_i$ implies that the rotation and magnetic moment vectors becomes nearly orthogonal. Annihilation cannot be complete if $\mu_1 \neq \mu_2$, and a remnant dipole must be left behind following the collision. The rotation of this remnant can be estimated by balancing the orbital angular momentum with the final spin angular momentum, $\mathcal{M} R_{\rm col} v \sim \mathcal{I}\Omega_f$, giving a final spin frequency

$$\frac{\Omega_f \mathcal{R}}{c} \sim f_{\rm em}^{1/3} \left(\frac{v}{c}\right)^{1/3}. \quad (10)$$

Assuming that the two colliding dipoles did not have nearly equal masses, this remnant rotational energy amounts to a fraction $\sim f_{\rm em}^{2/3}(v/c)^{2/3}$ of energy liberated in the collision.[2] It is lost to magnetic dipole radiation over the timescale

$$t_{\rm mdr} \sim \frac{\mathcal{I}c^3}{\mu^2\Omega_f^2} \sim f_{\rm em}^{-5/3}\left(\frac{v}{c}\right)^{-2/3}\frac{\mathcal{R}}{c} = \frac{10^2}{f_{\rm em}^{5/3} v_{7.5}^{2/3}}\frac{\mathcal{R}}{c}, \quad (11)$$

some 2-4 orders of magnitude longer than the width of the prompt electromagnetic pulse.

3. INTERACTION OF LSD WITH AMBIENT PLASMA

A single LSD moving through plasma at speed v excludes most of the ambient charged particles out to a radius

$$R_{\rm mag} \sim \left(\frac{\mu^2}{4\pi n_{\rm ex} m_p v^2}\right)^{1/6} = \frac{\mathcal{R}}{(v/c)^{1/3}}\left(\frac{\bar\rho_{\rm LSD}}{m_p n_{\rm ex}}\right)^{1/6}. \quad (12)$$

Here $n_{\rm ex}$ is the ambient number density of free electrons, and we define a characteristic density within a dipole radius $\mathcal{R}$,

$$\bar\rho_{\rm LSD} \equiv \frac{f_{\rm em}\mathcal{M}}{4\pi\mathcal{R}^3} = 8\times 10^{21}\, f_{\rm em}\mathcal{M}_{20}\mathcal{R}_{-1}^{-3} \quad {\rm g\ cm^{-3}}. \quad (13)$$

This 'magnetospheric' radius is much larger than the collision impact parameter (8), meaning that the vacuum approximation is well justified when treating the interaction between dipoles. In the case of a LSD moving through the interstellar medium at a speed $v \sim 10^{-3}\,c$, one finds $R_{\rm mag} \sim 400\, f_{\rm em}^{1/6}\mathcal{M}_{20}^{1/6}\mathcal{R}_{-1}^{1/2}$ km.

The hydromagnetic drag force acting on the LSD only slightly perturbs its orbit, unless $n_{\rm ex}$ is very high compared with a typical interstellar particle density. Writing

$$F_{\rm drag} = \frac{1}{2}C_d n_{\rm ex} m_p v^2 \cdot \pi R_{\rm mag}^2 \quad (14)$$

in terms of a drag coefficient $C_d = O(1)$ (e.g. Bailey & Hiatt 1972) one finds a drag time

$$t_{\rm drag} = \frac{\mathcal{M}v}{F_{\rm drag}} \sim \frac{8}{C_d f_{\rm em}}\left(\frac{\bar\rho_{\rm LSD}}{\rho_{\rm ex}}\right)^{1/2}\frac{R_{\rm mag}}{c}$$

$$= 2\times 10^{13}\, f_{\rm em}^{-1/3}\mathcal{M}_{20}^{2/3}\mathcal{R}_{-1}^{-1} n_{\rm ex,0}^{-2/3} v_{7.5}^{-1/3} \quad {\rm yr}. \quad (15)$$

The large majority of LSD orbits within galactic halos can therefore be treated as collisionless. Hydromagnetic drag clearly has a stronger effect on the rare LSD that happens to be accreted by a star (Section 7).

3.1. *Trapping by Supermassive Black Holes*

The hydromagnetic drag force just described opens up a new channel for trapping LSD near SMBHs, while avoiding accretion through the horizon.

A LSD orbiting a black hole experiences hydrodynamic drag even if its orbital angular momentum is aligned with the angular momentum of the gas accreting onto the hole. That is because a negative pressure gradient within the gas partly compensates the central gravitational field and causes the gas to rotate more slowly than a Keplerian orbit. Then an LSD in a circular orbit around a black hole of mass $M_\bullet$, with semi-major axis a and angular frequency $\Omega(a) = (GM_\bullet/a^3)^{1/2}$, experiences a headwind

$$\Delta v = \Omega a - \left(\Omega^2 a^2 + \frac{1}{\rho_g}\frac{dP_g}{\ln a}\right)^{1/2} \simeq -\frac{1}{2\rho_g\Omega}\frac{dP_g}{da}. \quad (16)$$

This headwind dies away where the radial pressure gradient vanishes, which happens just outside the ISCO as defined for material particles without drag. As a result, LSDs which experience strong enough drag to reach the inner part of the accretion flow will tend to collect in a narrow ring just outside the ISCO.

We now show that hydromagnetic drag acts on an inspiraling LSD over timescales intermediate between the orbital period and the age of the black hole. This means that the LSD is sensitive to a long-term average of the accretion flow, and will survive rapid ($\sim$ orbital period) turbulent fluctuations in the gas density and velocity fields. The inspiral may be concentrated in episodes of higher-than-average accretion, whereas the interaction between dipoles near the ISCO is spread out over longer intervals when the accretion rate is relatively low.

To simplify matters, we consider a radiatively inefficient and geometrically thick accretion flow with inflow speed $\alpha\cdot\Omega a$, where α is related to the usual viscosity coefficient (Shakura & Sunyaev 1973). Then the gas density needed to support a mass inflow rate $\dot M(a)$ is

$$\rho_g(a) = \frac{\dot M(a)}{\alpha\cdot 4\pi\Omega a^3} = \frac{\dot m(a)}{\varepsilon_{\rm rad}\alpha\kappa_{\rm es} a}\left(\frac{GM_\bullet}{ac^2}\right)^{1/2}. \quad (17)$$

Here $\kappa_{\rm es} \sim \sigma_T/m_p$ is the electron scattering opacity. The dimensionless accretion rate $\dot m = 1$ corresponds to the rate needed to power the Eddington luminosity $4\pi GM_\bullet c/\kappa_{\rm es}$ from an accretion flow with radiative efficiency $\varepsilon_{\rm rad}c^2$ per unit mass. The radial dependence of $\dot m$ is introduced to allow for a combined pattern of inflow and outflow, with plasma partly diverted from an accreting equatorial band into an outflowing polar wind (Blandford & Begelman 1999; Yuan et al. 2012). The gravitational radius is $R_g \equiv GM_\bullet/c^2$, so that, e.g., $\Omega(a) = (c/R_g)(a/R_g)^{-3/2}$.

[2] When $f_{\rm em} \ll 1$ one might imagine that additional components of the stress-energy of the dipoles could resist annihilation and prevent collisional energy release of the order of $\mathcal{M}c^2$. In fact, $f_{\rm em} \simeq 0.025$ for GUT-scale superconducting 'spring' loops. Then the magnitude of the prompt energy release depends on the relative sign of the currents on the colliding loops. It is $\sim f_{\rm em}\mathcal{M}c^2$ for loops with currents of like sign, and $\sim \mathcal{M}c^2$ for opposing signs. See the discussion in Section 5.

Substituting Equation (17) into Equation (15) gives

$$\Omega t_{\rm drag} \sim \frac{6\times 10^8}{(\Delta v/c)^{1/3}} \frac{f_{\rm hydro}\mathcal{M}_{20}^{2/3}}{\dot m(a)^{2/3} f_{\rm em}^{1/3}\mathcal{R}_{-1} M_{\bullet,7}^{1/3}} \left(\frac{a}{6R_g}\right)^{-1/2}, \tag{18}$$

or equivalently

$$t_{\rm drag} \sim 2.5\times 10^3 \frac{f_{\rm hydro}(\mathcal{M}_{20}\, M_{\bullet,7})^{2/3}}{\dot m(a)^{2/3} f_{\rm em}^{1/3}\mathcal{R}_{-1}} \left(\frac{a}{6R_g}\right)^{7/6} \quad {\rm yr}. \tag{19}$$

Here $M_{\bullet,7}$ is the black hole mass in units of $10^7\, M_\odot$. We factor out some properties of the accretion flow and the hydromagnetic interaction by defining $f_{\rm hydro} \equiv (\varepsilon_{{\rm rad},-1}\alpha_{-2})^{2/3} C_d^{-1}$.

Reconsidering now the effect of intermittent accretion on the trapped LSD ring, one recalls that a moderate fraction of the mass of $\sim 10^6$-$10^7\, M_\odot$ SMBHs may be build up by the tidal disruption of stars from the surrounding nuclear cluster Wang & Merritt (2004). The plasma density at the ISCO could easily increase by 6-7 orders during such an event, if the disrupted star had not yet left the hydrogen-burning main sequence. Nonetheless, one sees from Equation (18) that the drag time would remain longer than the orbital period. The essential feature of a pressure maximum near the ISCO would also be sustained during such an event, preventing an orbital instability of the LSD ring.

In the remainder of the paper, we first discuss the interaction between LSDs that are broadly distributed throughout galactic halos (Section 4) before turning to address their collisions near SMBHs (Section 6).

4. COLLISION RATE IN GALACTIC HALOS

We now consider the self-interaction of a LSD component of the cosmic cold dark matter (CDM). A first estimate shows that the optical depth to collisions *between* LSDs within a galaxy is very small. Consider a Milky Way type galaxy (halo mass $M_h \sim 1\times 10^{12}\, M_\odot$) with dark matter mass density $\rho_d \sim 3\times 10^{-24}$ g cm^{-3} at a galactocentric radius $R \sim 3$ kpc (e.g. Schaller et al. 2016). Magnetic dipoles are assumed to contribute a uniform fraction $f_{\rm LSD}$ of ρ_d. Then the optical depth to collisions between two dipoles is

$$\tau_{\rm col}(R) \sim \pi b_{\rm col}^2(\sigma) R \frac{\rho_d(R)}{\mathcal{M}}, \tag{20}$$

where $\sigma \sim 150$ km s^{-1} is the dark matter velocity dispersion. Substituting Equation (8) gives $\tau_{\rm col} \sim 1\times 10^{-18} f_{\rm LSD} f_{\rm em}^{2/3}\mathcal{R}_{-1}^2\mathcal{M}_{20}^{-1}$.

Given that only a percent of the halo dark mass is concentrated this close to the center of the galaxy, that the dark matter particles execute $\sim 10^3$ orbits over the Hubble time, and that 10 percent of the dark mass is bound in halos off mass $10^{12\pm 0.5}\, M_\odot$, one finds that a fraction $f_{\rm col} \sim \tau_{\rm col}(3\ {\rm kpc})$ of the LSD bound in halos will suffer a binary collision within a Hubble time. The rate out to a cosmological redshift $z \sim 1$ is

$$\Gamma_{{\rm col},z<1} \sim f_{\rm col}\cdot f_{\rm LSD}\Omega_{d,0}\frac{c^3}{G\mathcal{M}} \sim 8\times 10^4 f_{\rm LSD}^2 f_{\rm em}^{2/3}\mathcal{R}_{-1}^2\mathcal{M}_{20}^{-2} \quad {\rm day}^{-1} \tag{21}$$

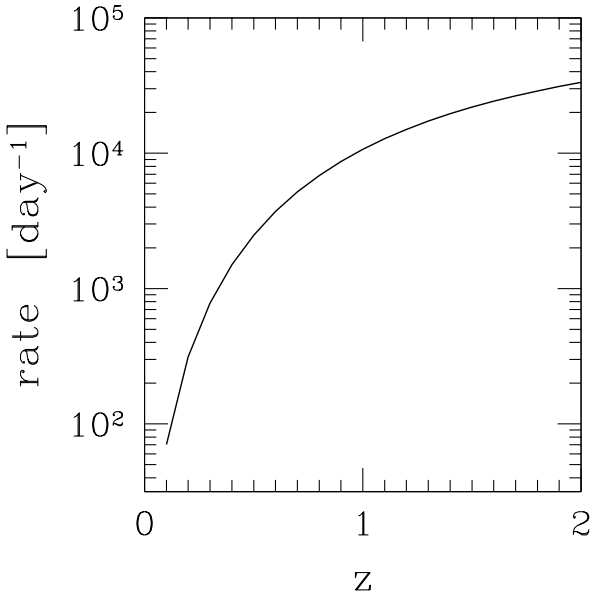

FIG. 3.— Cumulative rate of collisions between LSDs comprising the entirety of the cosmic dark matter ($f_{\rm LSD} = 1$), as a function of cosmological redshift. LSDs are assumed to have uniform mass $\mathcal{M} = 10^{20}$ g, radius $\mathcal{R} = 0.1$ cm, and $f_{\rm em} = 0.025$ as appropriate to superconducting 'spring' loops with tension $\mathcal{T} = 10^{-8}\, c^4/G$ (Section 5). The LSDs uniformly populate cold dark matter halos with masses exceeding $10^{10}\, M_\odot$ in a CMB-normalized cosmology. Halo profiles are NFW fits calibrated by the simulations of Klypin et al. (2011) and Prada et al. (2012). No correction is made for additional concentration of dark matter toward the centers of halos, resulting from the settling of gas.

in the standard ΛCDM cosmology with density $\Omega_{d,0} = \rho_d(0)/\rho_{\rm cr}(0) = 0.25$ of dark matter relative to the critical density at $z = 0$ (Planck Collaboration et al. 2016).

A more precise calculation of the collision rate is easily done by populating the universe with model dark matter halos. We use the mass distribution tabulated by Klypin et al. (2011) and the internal density profile of Navarro et al. (1997),

$$\rho_d(r, M_h, z) = \rho_{\rm cr}(z)\, \frac{\delta_c(M_h, z)}{(r/r_s)(1 + r/r_s)^2}, \tag{22}$$

as calibrated by Prada et al. (2012). Here $\rho_{\rm cr} = 3H(z)^2/8\pi G$, and the LSD space density is given by

$$n_{\rm LSD} = \frac{f_{\rm LSD}}{\mathcal{M}}\rho_d. \tag{23}$$

The scale radius $r_s = r_{200}/c$, compactness c, and normalization $\delta_c = 200c^3/3[\ln(1+c) - c/(1+c)]$ are all functions of halo mass M_h and redshift.

Here we avoid the complications arising from gas flows within forming galaxies and their influence on the central dark matter profile. Radiative settling of gas has the effect of compressing the dark matter near the centers of Milky-Way sized halos (e.g. Schaller et al. 2016), whereas persistent stirring of the baryons may smooth out the dark matter cusp at the center of dwarf halos (e.g. Governato et al. 2012). The strength of this second effect has been disputed (Fattahi et al. 2016). The overall sign of these effects on the LSD collision rate is

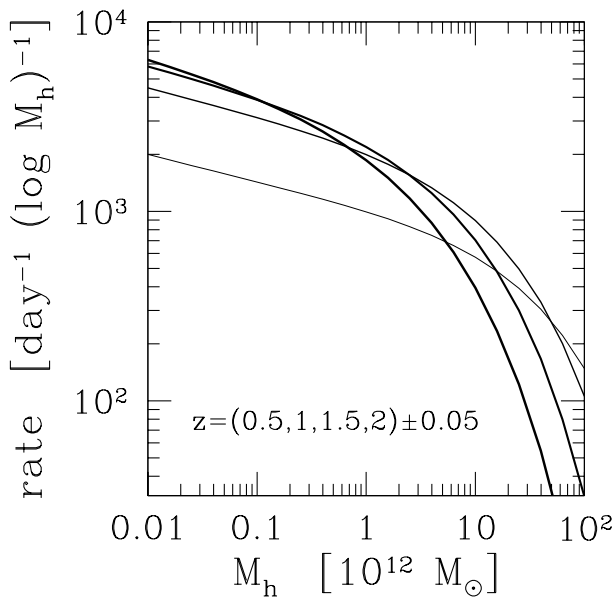

FIG. 4.— Differential rate of collisions between LSDs at redshifts $z = 0.5$, 1, 1.5, 2 (increasing line thickness) in the same calculation shown in Figure 3.

therefore unclear.

The LSD velocity distribution function is approximated as locally isothermal and isotropic, $f_{\rm LSD}(v) = f_0 e^{-v^2/2\sigma^2}$. The collision rate per unit volume is then obtained from the cross section (8) as

$$\frac{d\mathcal{R}}{dV} = \int d^3v_1 \int d^3v_2\, |\mathbf{v}_1 - \mathbf{v}_2|\, \sigma(|\mathbf{v}_1 - \mathbf{v}_2|)\, f(v_1) f(v_2) = \frac{2^{2/3}}{\pi^{1/2}} \Gamma\left(\frac{4}{3}\right)\, n_{\rm LSD}^2 \sigma \cdot \pi b_{\rm col}^2(\sigma). \quad (24)$$

The velocity dispersion profile of each halo is obtained by integrating the Jeans equation (Binney & Tremaine 2008)

$$\frac{r_s}{\rho_d}\frac{d(\rho_d\sigma^2)}{dr} = -\frac{GM_h(<r)}{r_s(r/r_s)^2} = -\frac{3}{2}(Hr_s)^2 \frac{\delta_c}{(r/r_s)^2} \times \left[\ln\left(1+\frac{r}{r_s}\right) - \frac{r/r_s}{1+r/r_s}\right]. \quad (25)$$

Finally the observed rate of potentially detectable LSD collisions is

$$\frac{d\Gamma_{\rm col}}{dz} = \frac{4\pi d_L(z)^2}{(1+z)^3}\frac{c}{H(z)}\left\langle \frac{d\mathcal{R}}{dV}\right\rangle (z). \quad (26)$$

Here a factor $(1+z)^{-1}$ accounts for cosmological time dilation, and the luminosity distance is $d_L(z) = (1+z)c\int dz/H(z)$. The average collision rate density $\langle d\mathcal{R}/dV\rangle$ at redshift z is obtained by integrating the volumetric rate (24) over the halo in each mass bin, and then summing over the halo mass function.

The cumulative distribution of collision rate with redshift is shown in Figure 4 for LSDs comprising the entirety of the dark matter ($f_{\rm LSD} = 1$), and with mass $\mathcal{M} = 10^{20}$ g, radius $\mathcal{R} = 0.1$ cm, and electromagnetic inertia parameter $f_{\rm em} = 0.025$ (as appropriate to 'spring' loops: Section 5). Here we include the contribution from all halos with masses exceeding $10^{10}\, M_\odot$. The result agrees with the preceding estimate (21). The differential contribution of halos of different masses at $z = 1$ is shown in Figure 4.

A more general dependence of $\Gamma_{\rm col}$ on dipole mass, abundance, and size is obtained from the scaling

$$\Gamma_{\rm col} \propto \left(\frac{f_{\rm LSD}}{\mathcal{M}}\right)^2 R_{\rm col}^2. \quad (27)$$

Changes in $\mathcal{M}$ still yield a fixed rate $\Gamma_{\rm col}$ if we also vary μ according to

$$\mu_{18}(\mathcal{M}, f_{\rm LSD}, \Gamma_{{\rm col},z<1}) = 1.5\, \frac{\mathcal{M}_{20}^2}{f_{\rm LSD}^{3/2}} \left(\frac{\Gamma_{{\rm col},z<1}}{10^4\ {\rm d}^{-1}}\right)^{3/4}\ {\rm G\,cm^3}. \quad (28)$$

Of course variations in detectability with explosion energy will modify this scaling.

When the LSD is composed of superconducting 'spring' loops, as described in Section 5, it turns out that the collision rate depends mainly on $f_{\rm LSD}$ and the string tension, not separately on $\mathcal{M}$ or μ.

Let us consider in more detail the dependence of $\Gamma_{\rm col}$ on the mass and energy density of the LSDs, or equivalently on the energy scale at which they formed in the early universe. Although LSD masses as light as $\mathcal{M} \sim 10^{18}$ g are consistent with FRBs of energy $\sim 10^{39}$ erg, the radiative efficiency is only modest, $\sim (2\pi\nu\mathcal{R}/c)^{0.5-1}$ at frequency ν (Paper I). The mass and radius normalizations we have chosen correspond, through Equation (1), to a magnetic field $\sim 10^{22} f_{\rm em}^{1/2}\mathcal{M}_{20}^{1/2}\mathcal{R}_{-1}^{-3/2}$ G, and an energy density $E_{\rm LSD}^4/(\hbar c)^3 \sim (20\ {\rm Gev})^4/(\hbar c)^3$. Expressing μ in terms of $E_{\rm LSD}$ and $\mathcal{M}$ shows that

$$\Gamma_{\rm col} \propto f_{\rm LSD}^2 \mathcal{M}^{-4/3} E_{\rm LSD}^{-8/3}. \quad (29)$$

Not surprisingly, higher $\mathcal{M}$ and $E_{\rm LSD}$ correspond to lower collision rates.

5. LSD AS A SUPERCONDUCTING 'SPRING' LOOP

The preceding considerations are illustrated here with a concrete example: loops of superconducting cosmic string carrying an electric current high enough to cancel off the string tension. Superconductivity in topologically stable, relativistic string defects was demonstrated by Witten (1985), under varying assumptions about the coupling of the carriers of ordinary electric charge to a Higgs field that breaks an additional $U(1)$ gauge symmetry. As the current flowing along the string grows in strength, the magnetic field winding around the string, and the kinetic energy of the charge carriers, together provide a rising positive pressure. It was conjectured by Ostriker et al. (1986), and demonstrated in detail by Copeland et al. (1987), Haws et al. (1988) and Davis & Shellard (1989), that closed loops of the string could form a stable, macroscopic form of dark matter due to a cancellation between the string tension and this positive pressure. If formed at sufficiently high redshift (associated, e.g., with symmetry breaking at a GUT en-

ergy scale $M_G c^2 \sim 10^{15}$-10^{16} GeV), these superconducting 'springs' could easily overclose the universe.

In fact, macroscopic superconducting 'spring' loops with a GUT-scale tension $\mathcal{T} \sim 10^{-8} c^4/G$ have just the relation between size and magnetic moment that we are looking for: a loop of radius $\mathcal{R}$ has a mass

$$\mathcal{M} \simeq \frac{2\pi\mathcal{R}\mathcal{T}}{c^2} = 8.5 \times 10^{19} \left(\frac{GT}{c^4}\right)_{-8} \mathcal{R}_{-1} \quad \text{g}. \tag{30}$$

The magnetic field scales inversely with distance ϖ from the string as $B_\phi(\varpi) = 2I/c\varpi$, meaning that a relatively weak field $2\mu/\mathcal{R}^3 \sim 10^{22}$ G is sustained at a macroscopic scale $\mathcal{R} \sim 0.1$ cm – as compared with the more substantial field ($\sim 10^{48-50}$ G) encountered in the string core. The one-dimensional pressure imparted by this field, integrated from the core to radius $\mathcal{R}$, is

$$\frac{dE_B}{d\ell} = \int_{R_G}^{\mathcal{R}} \frac{B_\phi^2(\varpi)}{8\pi} 2\pi\varpi d\varpi = \frac{I^2}{c^2}\Lambda \tag{31}$$

Here $R_G \equiv \hbar/M_G c$ and $\Lambda = \ln(\mathcal{R}/R_G) \sim 60 - 70$.

This large logarithmic factor greatly enhances the inertia of the loop, relative to the energy stored in the magnetic field at a scale $\sim \mathcal{R}$, which is approximately the magnetic dipole power $\sim \mu^2\mathcal{R}^{-3}$ that would be radiated during a collision between similarly sized loops. Adopting the parameterization (1), and noting that a circular loop carrying current I has a magnetic moment $\mu = \pi\mathcal{R}^2 I/c$, one finds

$$f_{\rm em} = \frac{\pi}{2\Lambda} \simeq 0.025. \tag{32}$$

The relation between loop mass and radiated electromagnetic energy $d\mathcal{E}_{\rm em}/d\ln\nu$ in a given band is obtained as follows. The initial pulse width is $\sim \mathcal{R}$ and the radiative efficiency at low frequency ν is $\sim (2\pi\nu\mathcal{R}/c)^{0.5-1}$ (that is, at a wavelength much larger than $\sim 2\pi\mathcal{R}$; Paper I). So, for example, for an index 0.5,

$$\frac{d\mathcal{E}_{\rm em}}{d\ln\nu} \sim \left(\frac{2\pi\nu\mathcal{R}}{c}\right)^{1/2} f_{\rm em}\mathcal{M}c^2$$
$$= 1 \times 10^{40}\, f_{\rm em} \frac{\mathcal{M}_{20}^{3/2}\nu_9^{1/2}}{[(G\mathcal{T}/c^4)_{-8}]^{1/2}} \quad \text{erg}. \tag{33}$$

There is an additional subtlety here arising from the sign of the current flowing along the string, relative to the longitudinal magnetic flux quantum threading its core. (This flux is associated with $U(1)$ gauge symmetry whose spontaneous breaking gives rise to the string defect.) Two gauged string loops of the same type always reconnect so that the direction of the core flux is continuous across the reconnection point. If their currents have the same relative sign, then it is easy to see that Equation (32) gives a good estimate of the ratio of radiated energy to rest energy of the colliding loops. Consider two 'spring' loops of equal sizes $\mathcal{R}$ and (necessarily) equal currents. The magnetic energy of each loop before the collision is, in a first approximation, $E_B = 2\pi\mathcal{R}(I/c)^2 \ln(\mathcal{R}/R_G)$. After the collision, the energy is $E_B = 2\pi(2\mathcal{R} + \delta\mathcal{R})(I/c)^2 \ln(2\mathcal{R}/R_G)$. Even in the absence of radiative energy loss during the collision, a small shrinkage $\delta\mathcal{R} \sim -\mathcal{R}/\Lambda$ is required to restore vanishing net tension.

The dissipation is much greater when the colliding 'spring' loops have currents with opposing signs. Now when the strings reconnect, the current develops strong inhomogeneities and zones with finite linear charge density ρ, even exceeding $|I|/c$ in magnitude in places. Here the electromagnetic field surrounding the string is predominantly electric, and one expects very strong dissipation. Collisions between loops with opposing currents should therefore produce explosions with a low-frequency electromagnetic precursor of energy similar to that radiated in the case of aligned currents, but followed by an intense thermal fireball. Now $f_{\rm em}$ represents the ratio of energies in these two components. The fireball can itself couple effectively to a propagating electromagnetic mode in the surrounding plasma (Blandford 1977, Paper I).

Next we consider the collision rate of superconducting 'spring' loops as a function of the string tension. Recall that the collision radius $R_{\rm col}$ is proportional to the radius $\mathcal{R}$ of the dipole but does not depend explicitly on its mass. Equation (27) then shows that the collision rate scales as $\Gamma_{\rm col} \propto f_{\rm LSD}^2(\mathcal{R}/\mathcal{M})^2$. But the string tension is approximately $\mathcal{T} \sim \mathcal{M}c^2/2\pi\mathcal{R}$, and so we find that $\Gamma_{\rm col} \propto (f_{\rm LSD}/\mathcal{T})^2$. The normalization works out to

$$\Gamma_{{\rm col},z<1} = 1 \times 10^4\, f_{\rm LSD}^2 \left(\frac{G\mathcal{T}/c^4}{10^{-8}}\right)^{-2} \quad \text{day}^{-1}. \tag{34}$$

The rate as a broader function of redshift is shown in Figure 3 for $f_{\rm LSD}^{-1}(G\mathcal{T}/c^4) = 10^{-8}$.

Our ab inito rate calculation can be compared with the measurement $\Gamma_{\rm FRB} = 3 \times 10^3$ d^{-1} for FRBs with fluence larger than $F_{\nu,\rm min} = 3.8$ Jy-ms at a frequency $\nu \sim 1.4$ GHz (Crawford et al. 2016). The curve in Figure 3 matches $\Gamma_{\rm FRB}$ at a cumulative emission redshift $z_{\rm max} \sim 0.55$. The rest-frame radio energy implied by a fluence $F_{\nu,\rm min}$ from a redshift $z_{\rm max}$ is $E_{\rm FRB} = 4\pi(1 + z_{\rm max})^{-1} d_L(z_{\rm max})^2 \nu F_{\nu,\rm min} \sim 4 \times 10^{40}$ erg. If this energy were supplied by the collision of two LSDs, then the mass implied by by Equation (33) is $\mathcal{M} \sim (1-2)\times 10^{20}$ g (again for $\mathcal{T} = 10^{-8}c^4/G$).

We note in closing that relativistic cusps forming on oscillating cosmic strings have long been known to be sources of intermittent bursts of gravitational and electromagnetic waves. In this case, the emitted electromagnetic pulse is significantly longer than a radio wavelength, so that the calculations of deceleration and radio wave emission in Paper I are not applicable. More broadly emission with a sub-millisecond duration, or emission repeating on a timescale of tens or hundreds of seconds, is not a natural outcome of GUT-scale string dynamics. A recent exploration in the context of FRBs has been made by Yu et al. (2014).

6. COLLISIONAL LSD RINGS TRAPPED NEAR SUPERMASSIVE BLACK HOLES

A competing, and perhaps dominant, channel for LSD annihilation involves SMBHs. This channel is made effective by a remarkable combination of properties of SMBHs: i) an enormous cross section to accrete ambient material, especially during a rapid growth phase; ii) the small volume of the space surrounding the hole, which permits a high optical depth to collisions between LSDs trapped there; and iii) the presence of gas dense enough

to drag LSDs into a narrow and long-lived ring just outside the ISCO.

6.1. *Adiabatic Compression of LSD Dark Matter around SMBHs Formed by Direct Gas Collapse*

We first estimate the net mass of LSD dark matter that would be compressed close enough to a SMBH to allow gas drag to take over and bring the LSDs close to the ISCO. This mass is maximized if the hole is assembled in situ in a galactic nucleus, in particular if most of its growth is due to hyper-Eddington accretion from a 10-100 pc sized plasma cloud (Loeb & Rasio 1994; Begelman et al. 2006). Dark matter permeating the nuclear region is adiabatically compressed as the black hole grows, with the strength of the compression depending on the relative increase in hole mass. The following considerations are therefore most relevant for the first generation of SMBHs, which might form in spheroids of mass $\sim 10^9\,M_\odot$ or smaller.

The dark matter is assumed initially to have formed a constant density core with central velocity dispersion σ_d. Once the SMBH has collapsed, its growth is filled out by continued radiative accretion, and hierarchical merging of with other dark matter halos brings the central stellar velocity dispersion up to the value implied by the measured $M_\bullet - \sigma$ relation (Gültekin et al. 2009). Consistent with this approach, we normalize σ_d to ~ 40 km s^{-1} for a $10^6\,M_\odot$ hole.

The gas profile around the nascent hole during the super-Eddington accretion phase is approximated by a singular isothermal sphere,

$$\rho_g(r) \sim \frac{\sigma_g^2}{2\pi G r^2}. \tag{35}$$

Here σ_g incorporates the contributions of turbulent, magnetic, and rotational stresses within the contracting gas, as well as strong radiation pressure. Collectively these stresses slow down the collapse compared with a thermally supported sphere. This type of structure is observed, with a normamlization $\sigma_g \sim 20$ km s^{-1}, in the gas+N-body simulations of low-mass galactic halos performed by Choi et al. (2013, 2015).

At the end of the prompt accretion phase, after the hole has developed and most of the gas around it has dissipated, the dark matter profile is given by (Peebles 1972; Young 1980)

$$\frac{\rho_d(r)}{\rho_{d,0}} = \frac{4}{3\pi^{1/2}}\left(\frac{GM_\bullet}{\sigma_d^2 r}\right)^{3/2}. \tag{36}$$

We normalize the initial central dark matter density $\rho_{d,0}$ in terms of a transition radius $R_{\rm gas}$ where $\rho_g(R_{\rm gas}) = \rho_{d,0}$. Then the mass profile of the dark matter cusp around the SMBH is

$$\frac{1}{M_\bullet}\frac{dM_d}{d\ln r_d} = \left(\frac{r_d}{R_g}\right)^{3/2}\frac{8G^2M_\bullet^2\sigma_g^2}{3\pi^{1/2}c^3\sigma_d^3R_{\rm gas}^2}$$
$$= 2\times 10^{-9}\left(\frac{r_d}{10^3\,R_g}\right)^{3/2}\frac{M_{\bullet,7}^2\sigma_{g,20}^2}{\sigma_{d,40}^3(R_{\rm gas}/10^2\ {\rm pc})^2}, \tag{37}$$

where $\sigma_{g,20} = \sigma_g/(20\ {\rm km\ s^{-1}})$, $\sigma_{d,40} = \sigma_d/(40\ {\rm km\ s^{-1}})$. We see that this process would allow $\sim 10^{12}$ LSD particles each of mass 10^{20} g to accumulate within $10^3\,R_g$ of a $10^7\,M_\odot$ SMBH.

The hydromagnetic drag experienced by the LSDs produces a strong enhancement in annihilation efficiency around a SMBH, as compared with dark matter composed of weakly interacting massive particles. In the latter case, one must assume that the initial dark matter profile is already centrally peaked (e.g. $\rho_d(r) \propto r^{-1}$: Navarro et al. 1997) in order to obtain an interesting WIMP annihilation rate (Gondolo & Silk 1999). (In this respect, relatively conservative assumptions underly our estimate of the LSD annihilation rate.) A sharper final dark matter cusp is also obtained if the initial orbits of the dark matter particles are circular (Steigman et al. 1978), but this density profile is not consistent with conservation of phase space density. Simulations by Capela et al. (2014) assuming a more isotropic initial phase space distribution produce a final density profile close to $\rho_d(r) \propto r^{-3/2}$, in agreement with the classic stellar dynamical result.

6.2. *Collisional Evolution of a LSD Ring Just Outside the ISCO*

Consider a large number N_d of LSDs that orbit in the equatorial plane of the black hole, near the radius where $dP_g/dr = 0$ in the accreting plasma flow. We ignore relativistic effects here and limit ourselves to a Newtonian treatment of the gravitational interactions of the dipoles. In this environment, gravitational stirring can be an important agent for growing random velocities. Expression (9) approximates the maximum random speed that can be reached by gravitational dipole-dipole scattering before it is limited by dissipative collisions.

The tidal force exerted by the SMBH has a negligible effect on LSD interactions when $v \gtrsim \Omega a(\mathcal{M}/M_\bullet)^{1/3} \sim 10^{-7}c\,\mathcal{M}_{20}^{1/3}M_{\bullet,7}^{-1/3}$. Then the scattering impact parameter of two dipoles each of mass $\mathcal{M}$ is $\sim 2G\mathcal{M}/v^2$. Balancing this with the collision radius (2) gives Equation (9).

We suppose that the dipoles placed near the ISCO initially feel strong enough drag that their orbits nearly circularize before two-body interactions become important. After this, the gas accretion rate is reduced, and the dipoles begin to interact gravitationally with each other. Their random velocity grows by gravitational scattering until it reaches the value (9), after which the number and mass of the dipoles is reduced by collisions mediated by the magnetic interaction.

The effective volume of the ring occupied by the LSDs is $V_{\rm ring} \sim 2\pi a\cdot\pi h^2 = \pi^3 a(v/\Omega)^2$. Approximating collisions as complete annihilations, the corresponding rate is

$$\dot{N}_d \sim -\frac{N_d^2}{V_{\rm ring}}\,\sigma_{\rm col}v. \tag{38}$$

Since v is independent of N_d but $\sigma_{\rm col}v \propto v^{-1/3}$ (Equation (8)), we obtain the scaling solution

$$N_d(t) \sim \frac{\pi^2}{3f_{\rm em}^{2/3}}\left(\frac{v}{c}\right)^{7/3}\left(\frac{a}{R_g}\right)^4\left(\frac{R_g}{\mathcal{R}}\right)^2\frac{R_g}{ct}$$

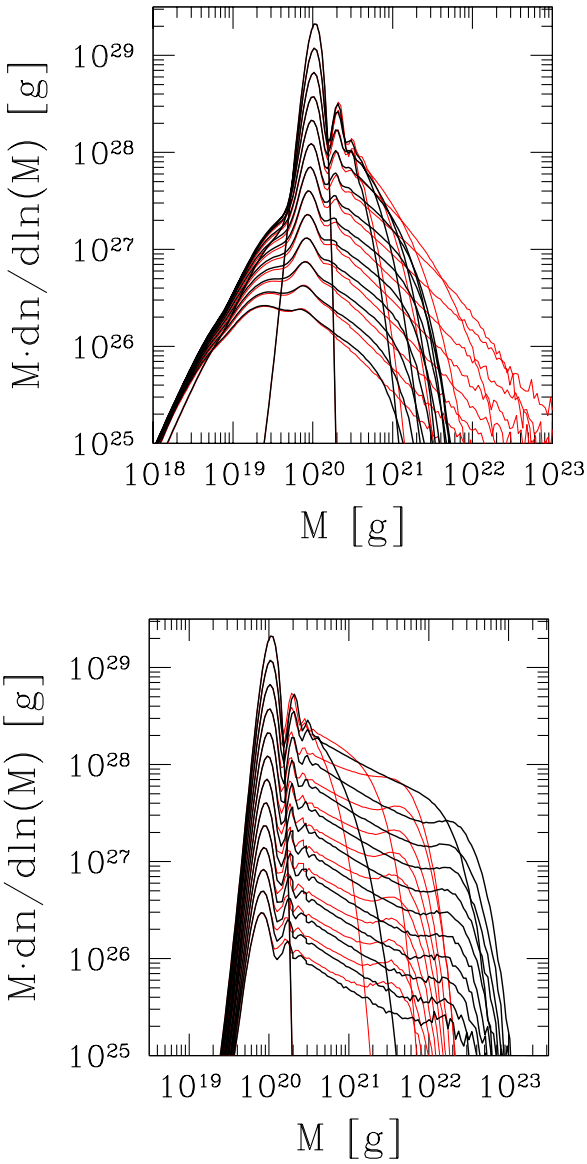

FIG. 5.— Collisional evolution of 10^9 dipoles trapped in a small volume, obtained from a direct Monte Carlo integration. Gaussian initial mass spectrum centered around $\bar{\mathcal{M}} = 10^{20}$ g. Cross section for collision between two dipoles of masses $\mathcal{M}_1 \neq \mathcal{M}_2$ and $\mu_1 \neq \mu_2$ is given by Equation (41). We treat separately two cases, appropriate to superconducting 'spring' loops, in which each loop has a random sign of $I \cdot \Phi_s$ (*top panel*) or ii) a fixed sign of $I \cdot \Phi_s$ (*bottom panel*). (Here I is the electric current flowingalong the string and Φ_s is the magnetic flux quantum (associated with a spontaneously broken $U(1)$ gauge symmetry) threading the string core.) Different line colors show the effect of varying the fraction $f_{\rm em}$ of the energy radiated in a given collision. Black curve: $f_{\rm em} = 0.025$ when the colliding loops have the same sign of $I \cdot \Phi_s$; otherwise (only in case i)) $f_{\rm em} = |\mathcal{M}_1 - \mathcal{M}_2|/(\mathcal{M}_1 + \mathcal{M}_2)$. Red curve: $f_{\rm em} \to 0$ (*top panel*); $f_{\rm em} \to 0.1$ (*bottom panel*).

$$= 3 \times 10^5 \, M_{\bullet,7}^3 \mathcal{M}_{20}^{7/4} \mathcal{R}_{-1}^{-15/4} \left(\frac{t}{\rm Gyr} \right)^{-1} \quad (39)$$

at $a \sim 6R_g$ and for $f_{\rm em} = 0.025$.

The steadily decreasing dipole number (39) is enhanced by a steady inflow of dipoles, say at a rate $\dot{N}_{d+}$. Balancing this source with annihilation gives the equilibrium number

$$N_{d,\rm eq} = 6 \times 10^7 \, M_{\bullet,7}^{3/2} \mathcal{M}_{20}^{7/8} \mathcal{R}_{-1}^{-15/8} \left(\frac{\dot{N}_{d+}}{10\,{\rm yr}^{-1}} \right)^{1/2} . \quad (40)$$

This result only holds at a sufficiently advanced time.

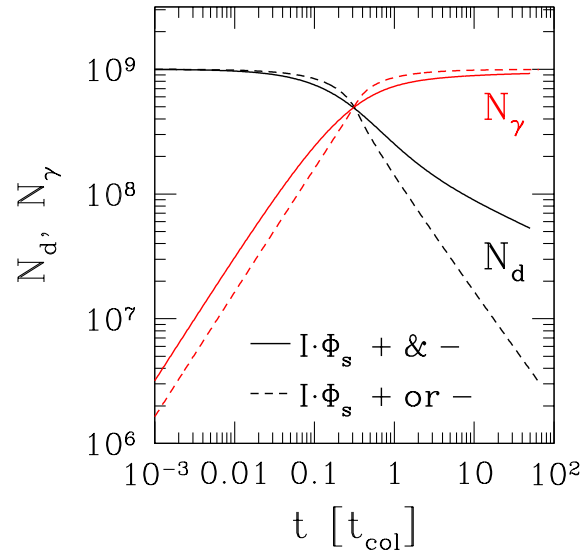

FIG. 6.— Rate of change of total dipole number N_d (black curves) and cumulative number of electromagnetic bursts N_γ (red curves) in the simulations of Figure 5. Time is scaled to collision time of two dipoles each of mass $\bar{\mathcal{M}}$ using Equation (38). Solid curves: case i) in which loops have both signs of $I \cdot \Phi_s$ with equal probability. Dashed curves: case ii) in which $I \cdot \Phi_s$ takes only one sign. Baseline $f_{\rm em} = 0.025$ in both cases. The decay of N_d is slower in case i) because the net dipole mass, and the collision cross section (41), drops in larger steps when loops of opposing signs collide.

6.3. *Collisional Evolution of the Dipole Mass Spectrum*

We now turn to the effects of collisions on the mass spectrum, and the energy distribution of radiated electromagnetic bursts that results. Start with a narrow initial distribution of $\mathcal{M}$ centered around some mass $\bar{\mathcal{M}}$ (Figure 5), with a corresponding magnetic moment $\bar{\mu}$. We focus on the specific case of superconducting 'spring' loops. These can exist in two configurations with $I \cdot \Phi_s > 0$ or < 0, where I is the electric current flowing along the string, and Φ_s is the magnetic flux quantum threading the string core.

The cross section for two dipoles with $\mu_1 \neq \mu_2$ is obtained by combining Equations (7) and (8), and assuming proportionality of μ and $\mathcal{M}$, as for a 'spring' of fixed tension $\mathcal{T}$.

$$\sigma_{\rm col}(\mu_1, \mu_2) = \sigma_{\rm col}(\bar{\mu}, \bar{\mu}) \frac{(\mu_1/\bar{\mu})^{1/3} \, (\mu_2/\bar{\mu})^{1/3}}{(2\mathcal{M}_r/\bar{\mathcal{M}})^{1/3}}$$
$$= \sigma_{\rm col}(\bar{\mu}, \bar{\mu}) \left(\frac{\mathcal{M}_1 + \mathcal{M}_2}{2\bar{\mathcal{M}}} \right)^{1/3} . \quad (41)$$

Here $\mathcal{M}_r = \mathcal{M}_1 \mathcal{M}_2/(\mathcal{M}_1 + \mathcal{M}_2)$ is the reduced mass.

Here we ignore the absolute normalization of time and dipole density. We start with a large number ($\sim 10^9$) of

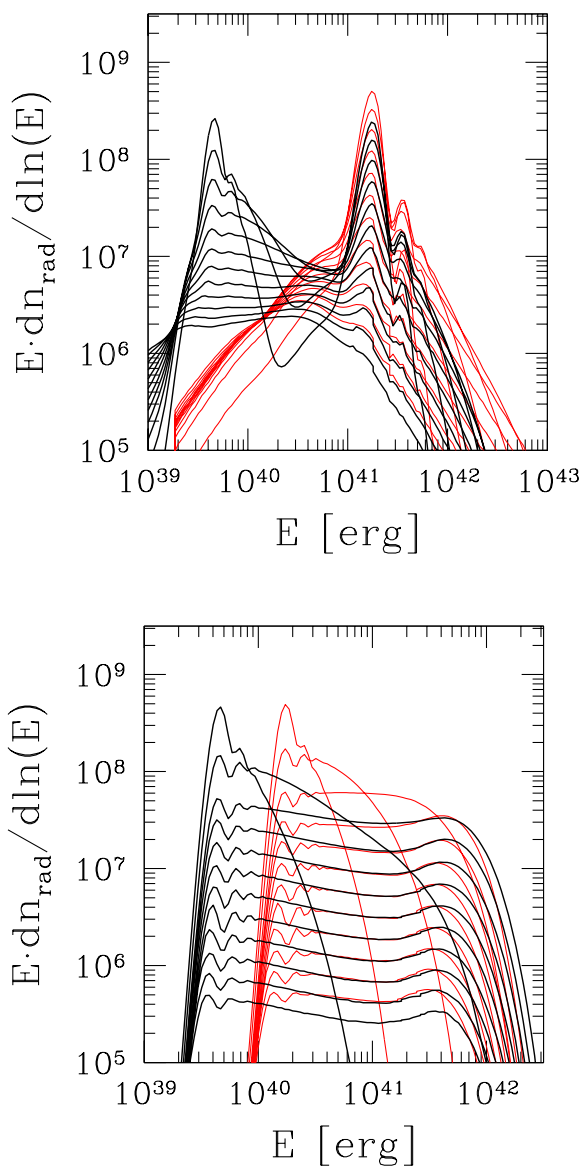

FIG. 7.— Distribution of bolometric energies of low-frequency electromagnetic bursts produced by collisions between dipoles in the simulations shown in Figure 5. *Top panel:* case i) with $I \cdot \Phi_s$ having random sign. *Bottom panel:* case ii) in which $I \cdot \Phi_s$ has uniform sign. Black curves: $f_{\rm em} = 0.025$. Red curves: $f_{\rm em} \to 0$ (*top panel*) and $f_{\rm em} = 0.1$ (*bottompanel*).

dipoles, evolving their mass distributions over a multiple of the collision time as defined by the initial configuration. The top panel of Figure 5 shows the result when equal numbers of both signs of $I \cdot \Phi_s$ are present in the initial condition. Collisions between loops of equal sign of $I \cdot \Phi_s$ create a loop whose mass is only slightly smaller than the sum, by a fractional amount $f_{\rm em} = 0.025$. The red curves show the effect of removing this small radiative loss ($f_{\rm em} \to 0$), but still allowing for the much stronger dissipation that results when loops of opposing signs collide. An extended power-law tail forms at high masses, which is truncated at a mass $\sim f_{\rm em}^{-1}\bar{\mathcal{M}}$ for finite $f_{\rm em}$.

A different result is obtained when only loops with one sign of $I \cdot \Phi_s$ are present (bottom panel of Figure 5). Now strongly dissipative mergers are absent, and finite $f_{\rm em}$ is required to prevent most of the mass from collecting in very large loops. As before, increasing $f_{\rm em}$ reduces the mass at which the high-energy tail cuts off.

Figure 6 shows how the number of loops decreases with time in the two cases. The decrease is slower when loops of both signs are present, because more small loops are formed which interact with a reduced cross section (41). This effect is evident in the distribution of electromagnetic pulse energies (Figure 7), which shows a main peak at an energy $\sim \bar{\mathcal{M}}c^2$ and a separate, lower-energy peak at $f_{\rm em}\bar{\mathcal{M}}c^2$. A much broader high-energy pulse energy tail is present when only loops of a single sign of $I \cdot \Phi_s$ are present (lower panel of Figure 7).

7. COLLISIONS WITH WHITE DWARF STARS

Stars of all types can collide with a LSD orbiting through the same galaxy. In contrast with small primordial black holes (PBHs), whose interactions with stars have been considered by Capela et al. (2013) and Graham et al. (2015), a trapped LSD cannot destroy its host by accreting it. But high temperatures are generated behind the shock that forms around the LSD during its supersonic motion through the star. In the case of a WD, one must consider whether this heating will trigger runaway thermonuclear burning. Graham et al. (2015) considered the interaction of small PBHs with WDs, finding a minimal size for the PBH that would trigger a carbon deflagation in WDs of various masses. The contribution of PBHs of mass 10^{20}-10^{22} g to the cosmic dark matter was found to be constrained by the observed rate of Type Ia supernovae.

Here we show that LSDs, of the mass and size needed to explain FRBs, will trigger thermonuclear deflagrations, and possibly direct detonations, in C/O WDs with masses exceeding $\sim 1\,M_\odot$. The collision probability is high for a star of mass $\sim M_\odot$ to experience such a collision if its lifetime exceeds a billion years, and if $f_{\rm LSD} = O(1)$. Heavier WDs with ONeMg composition have a somewhat higher threshold for ignition due to the stronger coulomb barrier in oxygen burning, with the result that only stars heavier than $\sim 1.29\,M_\odot$ are found to experience self-sustained burning. The initial spark is placed well off the center of the star in all cases, but especially in the more massive ONeMg models.

We first show that the hydromagnetic drag force overcomes gravity as the LSD moves through a dense and degenerate star (a WD or neutron star). Then the differential speed Δv between LSD and stellar material drops below the escape speed, except for trajectories that only touch the outermost layers.

We begin by evaluating the drag force (14) for a LSD on a ballistic trajectory midway through a target star of mass $M_\star$ and radius $R_\star$ (e.g. at a radius $\sim R_\star/2$ and local density $\rho_{\rm ex} \sim 3M_\star/4\pi R_\star^3$). The magnetic moment is expressed in terms of the string tension $\mathcal{T}$ (for a cosmic 'spring' loop), giving

$$\frac{F_{\rm drag}}{G\mathcal{M}M_\star/r^2} \sim 0.03\, C_d \left(\frac{G^2\mathcal{M}_{\rm rad}M_\star}{R_\star^2 c^4}\right)^{1/3} \left(\frac{G\mathcal{T}}{c^4}\right)^{-1}$$
$$= 0.02\, \frac{C_d \mathcal{M}_{\rm rad,20}^{1/3}}{(G\mathcal{T}/c^4)_{-8}} \left(\frac{M_\star}{M_\odot}\right)^{1/3} \left(\frac{R_\star}{R_\odot}\right)^{-2/3}.$$

(42)

One sees that a solar-type star may or may not supply enough drag to trap a LSD whose differential speed at infinity is $v_\infty \sim 0.3 v_{\rm esc}(R_\star) \sim 200$ km s^{-1}, where $v_{\rm esc}(R_\star) = (2GM_\star/R_\star)^{1/2}$ is the escape speed from the surface of the star. But the LSD will be trapped by a more compact star.

Consider in particular the interaction of a LSD with a WD composed mainly of carbon and oxygen. The rate of carbon burning is sensitive to temperature (Caughlan & Fowler 1988), and therefore to details of hydrodynamic response of the WD material. In contrast with an infalling PBH, the disturbance has a large enough scale that conductive heat transport is negligible. But we show that adiabatic cooling can have a dramatic effect: the burning rate drops precipitously as the shocked stellar material expands and returns to the ambient stellar pressure. The velocity shear established by the propagating shock can further suppress thermonuclear burning by triggering turbulence that mixes heat away from the center-of-mass trajectory of the LSD.

First we establish that the interaction between the LSD and the star is mainly hydromagnetic, not gravitational. In spite of the enormous difference in material density and magnetic field strength, there are similarities with the interaction between a planetary magnetosphere and the Solar wind. The gravity of the LSD by itself deflects the WD material only through a small angle

$$\frac{\Delta v_\perp}{\Delta v} \sim \frac{G\mathcal{M}}{R_{\rm mag}\Delta v} \sim 2\pi \left(\frac{G\mathcal{T}}{c^4}\right)\left(\frac{\Delta v}{c}\right)^{-7/3}\left(\frac{\bar\rho_{\rm LSD}}{\rho_{\rm wd}}\right)^{-1/6}, \tag{43}$$

which works out to $\Delta v_\perp/\Delta v \sim 10^{-3}(G\mathcal{T}/c^4)_{-8}$ for a LSD velocity $\Delta v \sim 10^3$ km s^{-1}. Here $\bar\rho_{\rm LSD}$ is given by Equation (13) and $\Delta v_\perp$ is the transverse impulse.

Peak temperature is reached behind the shock close to the center-of-mass trajectory of the LSD. The first thing to note is that this temperature only depends on the mass profile and gravity of the WD, as long as the LSD moves on a nearly ballistic trajectory. From Equation (15), we see that a LSD 'spring' with tension $\mathcal{T} \sim 10^{-8}c^4/G$ will experience drag inside a WD that is only moderately stronger than gravity. The internal energy density near the center of the WD increases rapidly with stellar mass, meaning that there is a critical mass above which self-sustained carbon (and oxygen) burning is triggered.

We proceed by introducing LSDs on downward Keplerian trajectories at the surface of a model WD, and then follow their radial and non-radial motion inside the star in response to the central gravity and drag force (14). The initial orbital angular momentum (impact parameter b) is scaled to the maximum value $\ell_{\rm col} = (2GM_{\rm wd}R_{\rm wd})^{1/2}$ that allows a direct collision with a star of mass $M_{\rm wd}$ and radius $R_{\rm wd}$,

$$\ell = b\Delta v_\infty = \left(\frac{b}{b_{\rm col}}\right)\ell_{\rm col}; \quad b_{\rm col} \equiv \frac{(2GM_{\rm wd}R_{\rm wd})^{1/2}}{\Delta v_\infty}. \tag{44}$$

The trajectory is characterized by ℓ, energy $\mathcal{E}$, and radial speed Δv_r. The energy is initialized to $\mathcal{E} = \frac{1}{2}\Delta v_\infty^2$, but the burning behavior is not sensitive to this choice for values of Δv_∞ characteristic of a galactic potential, being dominated instead by the stellar gravity. These quantities evolve according to

$$\frac{dr}{dt} = \Delta v_r = \pm 2^{1/2}\left[\mathcal{E} - \Phi(r) - \frac{\ell^2}{2r^2}\right]^{1/2};$$
$$\Delta v = 2^{1/2}\left[\mathcal{E} - \Phi(r)\right]^{1/2}; \quad \frac{d\Phi}{dr} = \frac{GM_{\rm wd}(<r)}{r^2};$$
$$\frac{d\mathcal{E}}{dt} = -F_{\rm drag}\Delta v; \qquad \frac{d\ell}{dt} = -F_{\rm drag}\frac{\ell}{\Delta v}. \tag{45}$$

Here $M_{\rm wd}(<r) < M_{\rm wd}$ is the mass enclosed inside radius $r < R_{\rm wd}$. The drag force evolves according to Equation (14) in response to changes in Δv and ambient mass density $\rho_{\rm ex} = \rho_{\rm wd}(r)$.

A sample trajectory of an infalling LSD particle (a superconducting 'spring' of mass 10^{20} g and tension $\mathcal{T} = 10^{-8}c^4/G$) spiraling through a $1.02\,M_\odot$ C/O WD is shown in Figure 8. The LSD impact parameter is $b_{\rm col}/\sqrt{2}$ and velocity at infinity $v_\infty = 200$ km s^{-1}.

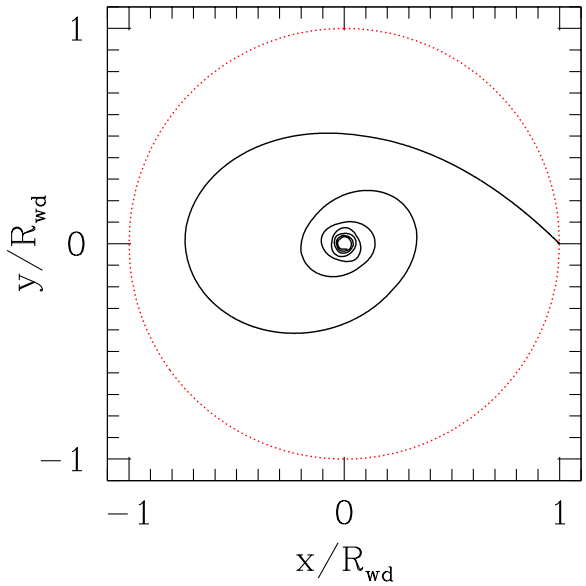

FIG. 8.— Sample trajectory of LSD 'spring' of mass 4×10^{20} g and tension $\mathcal{T} = 10^{-8}c^4/G$ falling throughaC/O WD of mass $1.02\,M_\odot$ and central density $10^{7.5}$ g cm^{-3}, in response to the stellar gravity and the hydromagnetic drag force (14). LSD velocity at infinity $\Delta v_\infty = 200$ km s^{-1} and impact parameter $b = b_{\rm col}/\sqrt{2}$. White dwarf surface is marked by the dotted red circle.

7.1. *Carbon Burning Behind the Shock*

To calculate the post-shock flow, we iteratively solve the equations of mass, momentum and energy conservation across the shock using the Helmholtz equation of state $P(\rho, T)$ based on a one-component plasma description of the ions (Timmes & Swesty 2000)

$$P_{\rm ps} + \rho_{\rm ps}v_{\rm ps}^2 = P_{\rm ex} + \rho_{\rm ex}\Delta v^2;$$
$$\frac{1}{\rho_{\rm ps}}\left(e_{\rm ps} + P_{\rm ps}\right) + \frac{1}{2}v_{\rm ps}^2 = \frac{1}{\rho_{\rm ex}}\left(e_{\rm ex} + P_{\rm ex}\right) + \frac{1}{2}\Delta v^2. \tag{46}$$

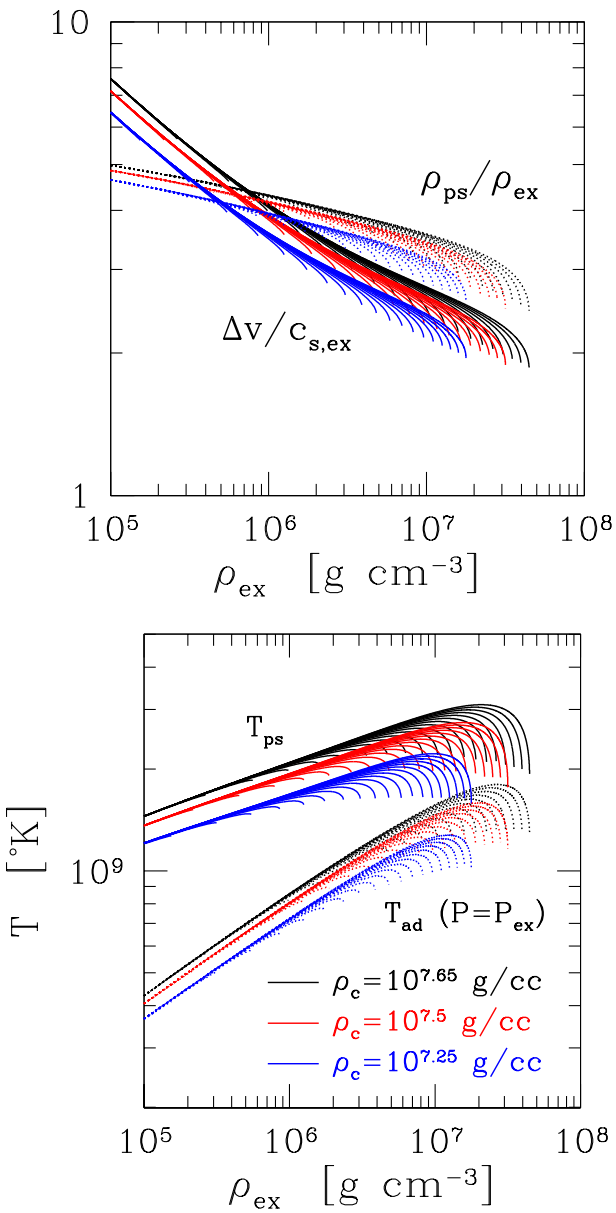

FIG. 9.— *Top panel:* Mach number and shock compression versus ambient stellar density for a LSD of mass $\mathcal{M} = 4 \times 10^{20}$ g and tension $\mathcal{T} = 10^{-8} c^4/G$. Each color shows a sequence of LSD trajectories with a range of impact parameters and a single C/O WD mass (black: central density $\rho_c = 10^{7.65}$ g cm^{-3} and mass $M_{\rm wd} = 1.07\,M_\odot$; red: $\rho_c = 10^{7.5}$ g cm^{-3} and $M_{\rm wd} = 1.02\,M_\odot$; blue: $\rho_c = 10^{7.25}$ g cm^{-3} and $M_{\rm wd} = 0.92\,M_\odot$). Squared impact parameter $(b/b_{\rm col})^2$ ranges linearly from 0 to 0.95 in steps of 0.05. Each trajectory is followed until the first radial turning point inside the WD, where v_r changes from negative to positive. Beyond this point, the LSD is slowed sufficiently that burning is inefficient. The top curve in each sequences corresponds to a zero angular momentum trajectory which reaches the center of the star on the first pass. *Bottom panel, solid curves:* post-shock temperature; *dotted curves:* temperature following adiabatic decompression to the ambient stellar pressure.

Here the subscript 'ps' denotes post-shock and $e_{\rm ps}$, $v_{\rm ps} = (\rho_{\rm ex}/\rho_{\rm ps})\Delta v$ are total internal energy per unit volume and velocity in the frame of the shock.

The mach number and compression at the head of the shock are plotted in Figure 9 (top panel) for a range of impact parameters, and for three WD models with central densities $10^{7.25}$, $10^{7.5}$, and $10^{7.65}$ g cm^{-3} (masses 0.92, 1.02 and 1.07 $M_\odot$). The shock is strong near the entry point (low stellar mass density), and begins to weaken near the first radial turning point, which coincides with the highest-density extension of the plotted curves. The shock remains relatively weak during the inspiral that follows, so that peak burning rates are reached before the first turning point.

In WD models expected to contain a significant abundance of carbon ($M_{\rm wd} \lesssim 1.07\,M_\odot$; Farmer et al. 2015), the peak post-shock temperature (bottom panel of Figure 9) is high enough to trigger strong carbon burning. However, the duration of peak compression is very short, only $\sim R_{\rm mag}/v_{\rm ps}$. We must therefore compare this hydrodynamic timescale, over which the shocked fluid decompresses back to the ambient stellar pressure, with the ignition time $t_{\rm ign,c+c}$ for carbon burning. The ignition time is defined here as the time to fully deplete the carbon, and we use the fitting formula for isobaric burning provided by Dursi & Timmes (2006). In practice the electrons in the shocked white dwarf material are only moderately degenerate, and one finds $t_{\rm ign,c+c} \sim 0.3 e_{\rm th,ps}/\rho_{\rm ps}\dot{\varepsilon}_{c+c}$, where $\dot{\varepsilon}_{c+c}$ the rate of energy release by carbon burning per unit mass, and $e_{\rm th}$ is the thermal energy density.

The top panel of Figure 10 shows that carbon burning significantly raises the internal heat of the shocked fluid in the heaviest (1.07 $M_\odot$) WD model, but not in the lightest model (0.92 $M_\odot$). In the first case, one can expect turbulent mixing of the heated carbon ashes with surrounding unburnt stellar material to trigger sustained burning. The 1.02 $M_\odot$ model just passes the threshold for sustained burning.

The next step is to follow the shocked fluid as it decompresses back to the ambient stellar pressure (bottom panel of Figure 10). First consider the case of slow post-shock burning. Approximating the decompression as adiabatic, one obtains the bottom set of temperature curves in Figure 9. In the 0.92 $M_\odot$ model, one finds that the energy input from burning drops below the loss from neutrino cooling.

It is also interesting to ask what happens when there is enough temperature growth to keep the heating rate within the decompressed fluid faster than neutrino cooling. Here it is important to keep in mind that the motion of the LSD through the star creates strong velocity shear transverse to this motion. Hydrodynamic turbulence will be excited by this shear, and provide greatly enhanced transport of momentum and heat away from the center-of-mass trajectory. This mixing process must slow down as the turbulent 'trail' expands, but it is limited by the stellar stratification only after it has reached the relatively large scale $\sim (rR_{\rm mag})^{1/2}$. This implies a strong dilution of the heat deposited by the shock, and it is plausible that self-sustained thermonuclear burning will not be attained unless strong burning occurs in the immediate post-shock flow. The range of C/O WD masses that experience sustained burning would be broadened

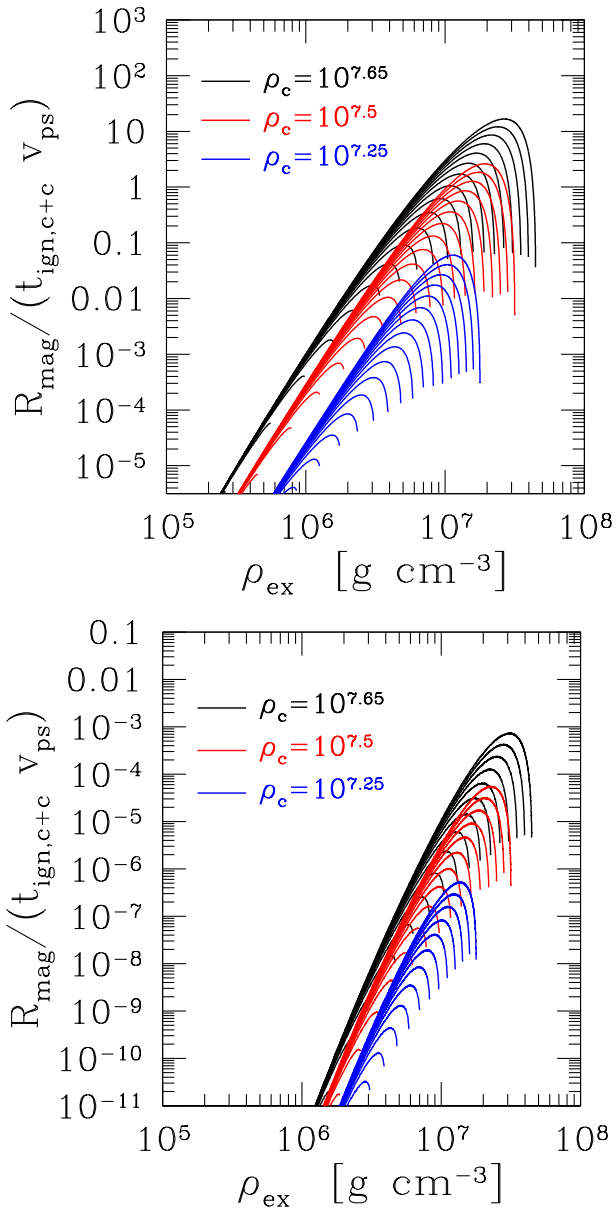

FIG. 10.— *Top panel:* Post-shock flow time $R_{\rm mag}/V_{\rm ps}$ compared with the ignition timescale $t_{\rm ign,cc}$ for carbon burning. WD is assumed to have equal mass fractions of carbon and oxygen. Colors and lines correspond to the same LSD trajectories and WD models as plotted in Figure 9. *Bottom panel:* Same as top panel, but now showing how adiabatic cooling from the post-shock condition down to the ambient stellar pressure decreases the rate of carbon burning. Each LSD shock trajectory is shown to a maximum density (minimum radius) corresponding to the first turning point.

slightly if this conclusion were incorrect.

7.2. *Oxygen Burning in Massive ONeMg WDs*

The calculations in the preceding Section were repeated for model WDs of ONeMg composition. The higher threshold temperature for runaway oxygen burning implies a higher mass threshold for the condition $t_{\rm ign,oo} = R_{\rm mag}/V_{\rm ps}$. We find that $M_{\rm wd} > 1.29\,M_\odot$ is required, with a weak dependence on the velocity-at-infinity of the infalling LSD.

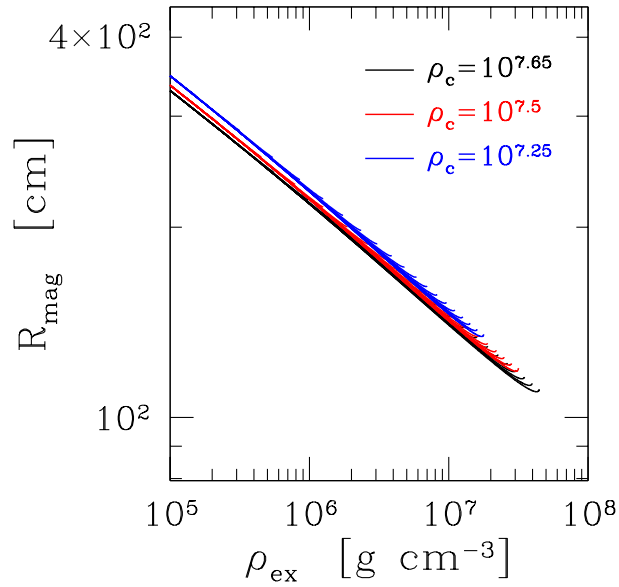

FIG. 11.— Magnetospheric radius $R_{\rm mag}$ (Equation (12)) of a LSD infalling through WDs of various masses. LSD and WD parameters are the same as in Figure 9 and 10.

7.3. *Off-Center Spark*

The long history of modeling thermonuclear explosions of WDs suggests that the observational consequences of a deflagration depend not only on the stellar mass, but also on the position of the initial spark. Figure 12 shows that this spark is situated at moderate depths when a LSD falls into a C/O WD of mass $1.0 - 1.07\,M_\odot$, but at relatively shallow depths for more mass ONeMg WDs heavier than $1.29\,M_\odot$. In fact, if the composition of the WD is fixed, then self-sustained burning is first triggered at lower *absolute* densities as the stellar mass is raised. That is because the greater compactness of the more massive WD implies a stronger drag at a given density.

7.4. *Prompt Detonation vs. Deflagration*

Does the shocking of WD material by an infalling LSD produce a deflagration (self-sustained burning by a turbulent flame) or a direct detonation (complete burning behind a propagating shock)? Complete burning within the hydrodynamic disturbance produced by the LSD (e.g. the top black curve of Figure 10) is not a guarantee that a detonation will be triggered. That is because a self-sustained detonation is suppressed by shock curvature (Niemeyer & Woosley 1997; Dursi & Timmes 2006). To evaluate the role of curvature here, we compare the magnetospheric radius $R_{\rm mag}$, shown in Figure 11 for the same trajectories and WD models as Figures 9 and 10, with the minimum hotspot size calculated by Dursi & Timmes (2006) (see their Equation 11):

$$R_{\rm det} = 1.63 \times 10^3\, \rho_{\rm ex,8}^{-1.22} \quad {\rm g\ cm^{-3}}. \qquad (47)$$

One sees that $R_{\rm mag}$ falls short of expression (47) by some two orders of magnitude at the density $\sim 10^7$ g cm^{-3} where burning is triggered in our C/O WD models (Figure 12). A related effect is that the shock speed (Figure 9) rises above the Chapman-Jouget speed (the

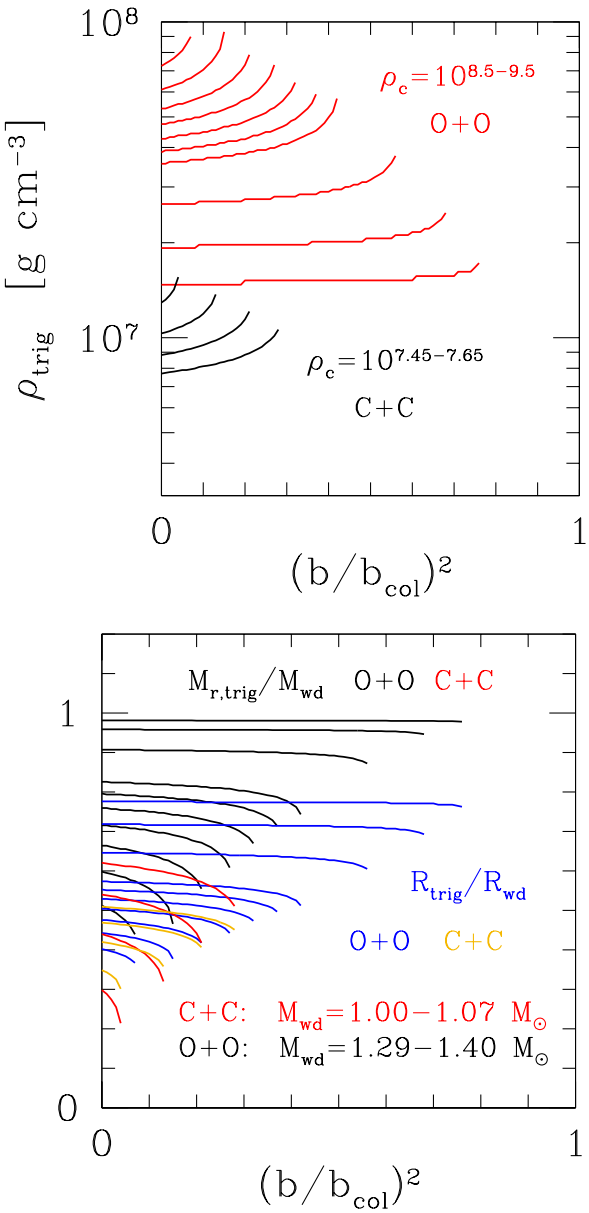

FIG. 12.— *Top panel:* Density at which sustained thermonuclear burning is first triggered along the trajectory of LSD falling into a WD. For a given composition, this density is *lower* for WD models of a higher mass and compactness, corresponding to a relatively large radius and enclosed mass. *Black lines:* cold C/O WD models of central density $10^{7.45-7.65}$ g cm^{-3}, increasing in steps of 0.05 in $\log_{10}\rho_c$. Corresponding WD masses range from 1.0 to 1.07 $M_\odot$. *Red lines:* ONeMg WDs of central density $10^{8.5-9.5}$ g cm^{-3}, increasing in steps of 0.05 and then 0.25 in $\log_{10}\rho_c$. Corresponding WD mass ranges from 1.29 to 1.40 $M_\odot$. *Bottom panel:* Outer radius $R_{\rm trig}$ and enclosed mass $M_{r,\rm trig}$ of sustained burning.

approximate propagation speed of a self-sustained detonation) at the point of strongest burning. As a result, the standoff of the shock from the magnetospheric boundary of the LSD cannot be strongly inflated by the heat input from burning.

We conclude that the disturbance produced by an infalling LSD results in localized production of iron group elements in $1.0-1.07\,M_\odot$ WDs, but the case for a prompt detonation is uncertain. The spark has a very different (approximately cylindrical) geometry to that usually assumed.

This (admittedly exotic) process gives a concrete example of an interesting problem which deserves further exploration through simulation: impulsive and directional forcing of thermonuclear burning, as opposed to triggering by an initially static hotspot (the more commonly considered problem).

We discuss the implications of this triggering model for iron group nucleosynthesis, the Type Ia supernova rate, and the nature of the Type Ia progenitors, in the concluding Section 8.8.

8. CONCLUSIONS AND PREDICTIONS

We have described the collisional properties of primeval magnetic dipoles of ~ 1 mm size and mass $\sim 10^{20}$ g in an evolving cold dark matter dominated universe. The cross section for free classical dipoles to collide has been calculated. If such LSDs comprise a significant component of the dark matter then their collisions produce intense, low-frequency electromagnetic pulses at a rate consistent with the observed rate of FRBs. Superconducting 'spring' loops with tension $\mathcal{T} \sim 10^{-8}c^4/G$ are an interesting microphysical candidate for LSDs. Young SMBHs forming by direct collapse of gas in dark matter halos of medium mass will be surrounded by long-lived collisional rings of LSD. These objects are repeating sources of FRBs, and may dominate the global rate. The mass distribution of LSDs is significantly modified by repeated collisions in such an environment. We apply our results to the repeating and recently localized source FRB 121102.

There are a number of additional observational constraints on LSDs, and interesting consequences of the web of physical processes examined here. These include a promising application to the triggering of thermonuclear explosions of WDs colliding with LSDs: the same LSD properties that explain the energies and rates of FRBs also imply an explosion rate of $> 1\,M_\odot$ WDs, and a corresponding yield of ^{56}Fe, that are remarkably close to those of Type Ia supernovae.

In addition, the cosmic abundance of LSDs is squeezed from above the mass range preferred for FRB emission by microlensing constraints, and from below by a high rate of disruptive collisions with WD stars. We make testable predictions of bright and narrow bursts at high (~ 100 GHz) frequencies associated with nearby supermassive black holes, and note that μJy level radio emission with enormous proper motion is potentially detectable from the closest LSDs moving at high speed through the outer Solar system. The approach to the FRB puzzle advanced here is testable from multiple directions.

8.1. *Constraints from Host Dispersion Measure, Rotation Measure, and Pulse Scattering Broadening*

An intense GHz electromagnetic pulse with energy $\sim 10^{39}$ erg can avoid synchrotron absorption within the inner accretion flow of a SMBH (mass $M_\bullet$) by raising the energies of the flow electrons. Plasma dispersion in such a dense medium spreads out the pulse in the propagation direction, thereby reducing the relativistic quiver radius

to

$$R_{\mathrm{rel},\omega} \sim \left(\frac{\omega \mathcal{E}_\omega}{4\pi n_e m_e c^2}\right)^{1/3} = 4.6\times 10^{12}\,(\omega\mathcal{E}_\omega)_{39}^{1/3} n_{e,6}^{-1/3} \quad \mathrm{cm} \qquad (48)$$

(Equation (120) of Paper I). In our approach to the emission mechanism, the effect is dominated by the peak of the spectrum at $\sim 10^2$ GHz, where one may expect $\omega\mathcal{E}_\omega$ to reach 10^{40-41} erg.

The wave grows too weak to induce relativistic motion at the radius (48). Synchroton absorption of GHz photons can be avoided in the relatively undisturbed accretion flow just outside this point if

$$n_{e,\mathrm{ISCO}} < 2\times 10^7\,\nu_9^{8/9}(\omega\mathcal{E}_\omega)_{41}^{4/9} M_{\bullet,6}^{-14/9} \quad \mathrm{cm}^{-3} \qquad (49)$$

(Equation (132) of Paper I). This estimate is based on recent models of radiatively inefficient accretion flows (RIAFs) which find a profile $n_e(r) \propto r^{-1}$ in between the Bondi radius R_B and the ISCO, with the heated electrons become non-relativistic at a distance $R_{\mathrm{rel}} \sim 200 R_g$ from the hole (Yuan et al. 2003, 2012).

8.1.1. *Dispersion*

The accretion flow will therefore contribute negligibly to the dispersion measure (DM) of observable FRBs emitted by LSD collisions near the ISCO of a SMBH (compare with the observed DM $\sim$ 300-500 cm^{-3} pc):

$$\mathrm{DM} \sim n_{e,\mathrm{ISCO}} R_{\mathrm{ISCO}} \ln\left(\frac{R_B}{R_{\mathrm{rel}}}\right) \sim 10\, n_{e,\mathrm{ISCO},7} M_{\bullet,6} \quad \mathrm{cm}^{-3}\ \mathrm{pc}. \qquad (50)$$

Here $R_B \sim 1\times 10^{17} M_{\bullet,6}$ cm given a plasma temperature ~ 1 keV in the circumnuclear region.

8.1.2. *Faraday Rotation*

Strong linear polarization is a natural consequence of the three emission channels for a superluminal electromagnetic wave that are described in Paper I. The starting point is a relativistic, magnetized shell with a dilute gas of embedded warm $e^\pm$ pairs that was created during a collision between LSDs. A superluminal wave is emitted by

1. Direct linear conversion of the magnetic field embedded in the shell;

2. Reflection of an ambient magnetic field by the surface of the conducting shell (see also Blandford (1977) for a discussion of radio emission from exploding black holes);

3. Excitation of an electromagnetic wave by the corrugated shell surface, with the corrugations being triggered by reconnection of the shell magnetic field with an ambient field.

A relatively large rotation of this linear polarization would be produced by propagation through the surrounding RIAF. The contribution to the rotation measure (RM) from the RIAF is concentrated at radius $\sim R_{\mathrm{rel}}$. Given that the magnetic pressure scales as a constant fraction of the thermal electron pressure ($\sim r^{-2}$), one gets

$$\mathrm{RM} \sim 10^6\, n_{e,\mathrm{ISCO},7} M_{\bullet,6} \left(\frac{R_{\mathrm{rel}}}{10^3\, R_g}\right)^{-1/2} \quad \mathrm{m}^{-2}. \qquad (51)$$

This appears to be near the threshold of detectability of existing FRB measurements; a much larger RM would presumably cause depolarization at $\sim$ GHz frequencies.

An important test of these ideas comes from FRBs which show low RMs, the main example so far being FRB 150807 (Ravi et al. 2016). Our approach requires that these events arise from LSD collisions in galactic halos, far removed from SMBHs. Unless a mechanism can be found for suppressing the accretion rate onto a SMBH well below the already low level of Sgr A*, there is a strong requirement that a FRB showing low RM will not repeat.

By the same token, the absence so far of detected polarization in the repeating bursts of FRB 121102 requires Faraday depolarization.

8.1.3. *Scattering Delay*

Although a high level of turbulence is expected within a RIAF, the scattering delay of an electromagnetic pulse emitted in its inner parts would be suppressed by the short path length:

$$\delta t \sim \frac{1}{2}\left(\frac{\omega_{Pe}}{\omega}\right)^4 \frac{r}{c} \sim 0.3\, n_{e,\mathrm{ISCO},7}^2 \nu_9^{-4} M_{\bullet,6} \quad \mu\mathrm{s}. \qquad (52)$$

The dominant contribution comes once again from radius $\sim R_{\mathrm{rel}}$. Here we have normalized $n_{e,\mathrm{ISCO}}$ to the limiting value (49) allowed by synchrotron absorption.

8.2. *Repetitions – Application to FRB 121102*

We now describe how the results reported in this paper and Paper I may be applied to the repeating FRB 121102. This source has been localized to a low-mass dwarf galaxy at redshift 0.19 (Tendulkar et al. 2017), and appears to sit within $\sim$ 40 pc of a compact radio source (Marcote et al. 2017; Chatterjee et al. 2017).

Obtaining FRB repetitions by the radiation mechanism advanced here must involve a very compact cloud of LSD. This we suggest forms most easily by direct collapse of gas combined with a small amount of dark matter into a SMBH (Section 6). It is natural to identify such a SMBH with the radio counterpart of 121102. The low stellar mass ($\lesssim 10^8\, M_\odot$) of the host galaxy of FRB 121102 suggests that this SMBH is of modest mass, $\lesssim 10^6\, M_\odot$. Equations (39) and (40) then show that the annihilation rate of LSDs has relaxed to the equilibrium inflow rate as determined by gas drag.

We require a low present accretion rate onto the black hole for the high-amplitude radio pulses to escape unattenuated. Indeed, a SMBH mass below $10^6\, M_\odot$ could significantly improve the transparency of the accretion flow, as described in Section 8.1. Although the radio source around the SMBH could not be powered by the present accretion, one recalls that strongly intermittent accretion onto Sgr A* has been inferred from measurements of X-ray reflection, with a major outburst occuring within the last $\sim 10^2$ yr (Churazov et al. 2017). The radio source associated with FRB 121102 could represent persistent synchrotron emission from a similarly recent outburst.

We suppose that the SMBH has been accreting dark matter from an adiabatically contracted cusp for a time $t_{\rm SMBH}$. The density profile of this cusp is given by Equation (36). We set the outer radius $r_{d,\rm acc}$ of the accreted dark matter particles by equating $t_{\rm SMBH}$ with the drag time (19), finding

$$\frac{r_{d,\rm acc}}{R_{\rm ISCO}} = 1.8\times 10^4 \left(\frac{t_{\rm SMBH}}{3\ {\rm Gyr}}\right)^{6/7} \frac{f_{\rm em}^{2/7}\mathcal{R}_{-1}^{6/7}\dot m_{-3}^{4/7}}{f_{\rm hydro}^{6/7}\mathcal{M}_{20}^{4/7}M_{\bullet,6}^{4/7}}. \tag{53}$$

Here $\dot m$ is the long-term average of the accretion rate onto the SMBH, as measured in terms of the Eddington rate. The long-term average of the inflow rate of LSDs to the ISCO is, then,

$$\begin{aligned}\dot N_{d+} &= \frac{1}{t_{\rm SMBH}\mathcal{M}}\frac{dM_d}{d\ln r_d}\bigg|_{r_{d,\rm acc}} \\ &= 5\left(\frac{t_{\rm SMBH}}{3\ {\rm Gyr}}\right)^{2/7}\frac{M_{\bullet,6}^{15/7}\dot m_{-3}^{6/7}f_{\rm em}^{3/7}\mathcal{R}_{-1}^{9/7}}{f_{\rm hydro}^{9/7}\mathcal{M}_{20}^{13/7}}\quad {\rm yr}^{-1}.\end{aligned} \tag{54}$$

Here we have normalized the seed mass profile during the early gas collapse phase to $\sigma_d = 40$ km s^{-1}, $\sigma_g = 20$ km s^{-1} and transition radius $R_{\rm gas} = 100$ pc between gas and dark matter (Equation (36)).

A supply rate of ~ 10 yr^{-1} of LSD to a SMBH in the FRB 121102 host may be too small, given the modest duty cycle of the radio monitoring, even allowing for repetitions produced by gravitational lensing and reflection off dense plasma (Section 8.2.1). The LSD mass normalization made in this estimate corresponds to a GHz burst energy $\sim 10^{39}$ erg, and could easily be reduced by an order of magnitude in this environment. We showed in Section 6 that repeated collisions between LSDs orbiting the SMBH create a high-energy tail to the burst energy distribution. Substituting $\mathcal{M}\sim 10^{19}$ g in Equation (54) then implies an increase to several hundred bursts per year. There are, however, compensating constraints associated with an increased collision rate with WD stars (Section 8.8.1).

8.2.1. *Repetition Timescales*

Repetitions from FRB 121102 do not appear to happen in a Poissonian manner. A lower timescale for repetition is obtained from the differential gravitational lensing delay, which is of the order

$$\Delta t_{\rm lens} \sim \frac{R_{\rm ISCO}}{c} = 30\, M_{\bullet,6}\quad {\rm s}. \tag{55}$$

This is comparable to the shortest repetition period observed from FRB 121102 (22.7 seconds; Spitler et al. 2016) for a $\sim 10^6\, M_\odot$ black hole.

Longer repetition periods are made possible by a geometrical delay associated with reflection. There are several strong constraints on reflection as a source of bright and narrow FRB 'afterimages', all of which are plausibly satisfied by an accretion flow onto a SMBH.

1. The radius of curvature R_c of the mirror must be comparable to its separation D_{sm} from the FRB source. Otherwise the brightness of the reflected pulse is greatly diluted, by a factor $\sim (R_c/D_{sm})^2$.

2. The plasma density must reach

$$n_{e,\rm ref} \sim 1\times 10^{10}\theta_{\rm ref}^2\nu_9^2\quad {\rm cm}^{-3} \tag{56}$$

in order to reflect GHz radiation through an angle $\theta_{\rm ref}$.

Neither of these constraints is readily satisfied by an intervening plasma cloud within the host galaxy. By contrast, a warm accretion disk orbiting a SMBH can easily reach such a density, and a warped disk naturally has curvature radius $R_c\sim D_{sm}$ at a distance D_{sm} from the hole. Of course, the reflection density (56) greatly exceeds the maximum n_e (49) that would allow the pulse to escape from the ISCO. This might point to 'magnetic arrest' of the innermost accretion flow by a concentrated magnetic flux bundle, to a two-phase structure of the flow, or to a radial transition from an outer thin disk to an inner hot and slowly cooling RIAF (Section 8.3).

3. Reflection cannot occur too close to the FRB source: electrons overlapping the pulse are heated to $\langle\gamma_e\rangle \gtrsim m_p/4m_e$ inside the radius $R_{{\rm rel},\omega}\sim 10^{13}$ cm (Equation (48)). A characteristic geometric delay is then $R_{{\rm rel},\omega}/c \gtrsim$ 300-1000 s. This is, interestingly, comparable to the duration of two clusters of GHz pulses detected from FRB 121102 (Spitler et al. 2016; Scholz et al. 2016).

Such a transition to a subrelativistic electron motion could begin only after the electromagnetic pulse begins to overlap an intervening dense plasma screen. Placing the screen at a distance $D_{sm} = 10^{13}$ cm from the FRB, the transition begins after the $\sim$ 0.01-1 THz forward pulse penetrates to a column $\delta N_e \sim \omega\mathcal{E}_\omega/4\pi R_s^2 m_e c^2 = 1\times 10^{20}(\omega\mathcal{E}_\omega)_{41}D_{sm,13}^{-2}$ cm^{-2} below the disk surface, with non-relativistic electron energies being reached at a column $\ln(m_p/4m_e)\sim 6$ times greater (see Equation (127) of Paper I).

This approach to repetitions in FRB 121102 is testable with upcoming monitoring. Repetitions on a timescale much less than ~ 10 s, but much longer than a few ms, would invalidate the hypothesis of gravitational lensing. One should also observe a significant gap in the repetition interval between the lensing time (55) and the minimum propagating time of a few hundred seconds to a non-relativistic plasma mirror.

8.3. *Pulse Broadening During Reflection*

In addition to the overall geometric delay, reflection creates a differential delay between neighboring frequencies. If the electrons in the screen remained subrelativistic, this would potentially add to the dispersion measure in excess of the $\sim \delta$DM $\sim$ 3-10 cm^{-3} pc limit imposed by pulse-to-pulse measurement variations in FRB 121102. There would also be a differential delay (Figure 13) associated with the greater penetration of higher frequencies into the mirror. For example, in an isothermal atmosphere with scaleheight h, the geometric delay between frequencies ω, $\omega+\delta\omega$ is

$$\delta t_d = 4\frac{h}{c}\ln\left(1+\frac{\delta\omega}{\omega}\right) \tag{57}$$

in the case of normal incidence. This only approximates a (negative) plasma dispersion over a narrow band. Making that correspondence between h and δDM, and demanding that the geometric delay not cause a measurable deviation from the cold plasma dispersion law at finite

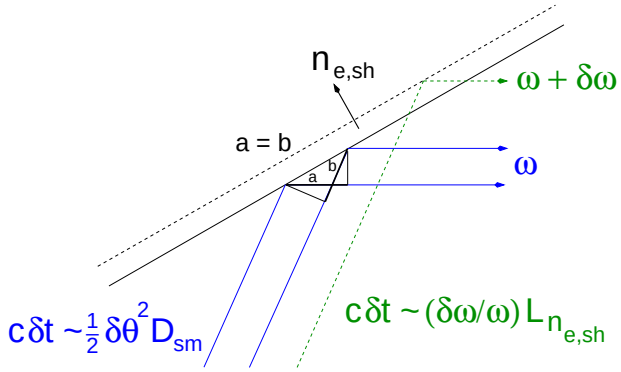

FIG. 13.— Differential delay experienced by a collimated electromagnetic pulse reflecting off a plasma screen at a distance D_{sm} from the FRB, relative to the mean geometric delay $t_d = \frac{1}{2}\theta_{\rm ref}^2 D_{sm}/c$. At a fixed frequency (blue rays) the delay is dominated by the curvature of the wavefront. The angle $\delta\theta$ has contributions from the finite emission size ($\delta\theta \sim \Gamma_{\rm em}^{-1} m$, where $\Gamma_{\rm em}$ is the Lorentz factor of the magnetized shell at the emission point, and m is the magnification of the source by the mirror) and from corrugations of the mirror surface. The differential delay between neighboring frequencies is dominated by the electron density gradient within the mirror. Here it is essential to take into account the energization of electrons in the mirror by a narrow 0.01-1 THz precursor of the GHz pulse. A rapid transition from relativistic to non-relativistic electron energies occurs at an electron column $\sim 10^{20}$ cm^{-2} for a mirror-FRB displacement $D_{sm} \sim 10^{13}$ cm. Here $n_{e,\rm sh}$ is the electron density in the plasma screen, and L_{n_e} its gradient scale normal to the screen.

bandwidth ($\delta\nu/\nu \sim 0.4$ in the Arecibo observations of FRB 121102: Scholz et al. 2016), one would require the scale height to be smaller than

$$h < \frac{e^2}{4\pi m_e \nu^2}\delta{\rm DM} = 6\times 10^8\ \nu_9^{-2}\left(\frac{\delta{\rm DM}}{10\ {\rm cm}^{-3}\ {\rm pc}}\right)\quad {\rm cm}. \tag{58}$$

The scalelength of the plasma frequency variation is slightly shortened by the transition of the electrons from relativistic to sub-relativistic motion within the strong electromagnetic pulse, by a factor $\sim 1/\ln(m_p/4m_e)$. Combining this effect with Equation (58), a rough upper bound on h is $\sim 10^9$ cm for a 2 GHz pulse.

Such a small scaleheight at the relatively low column $N_e \lesssim 10^{20}$ cm^{-2} is clearly inconsistent with a magnetically active accretion disk, in which the magnetorotational instability would generate a warm corona with a larger column. However, an accretion disk feeding a SMBH has a relatively low effective temperature, so that mid-plane temperatures below $\sim 10^4$ °K may be reached at $\sim 10^2 - 10^3$ gravitational radii and low accretion rates. Such a weakly ionized disk could hibernate in a state reminiscent of the quiescent states of cataclysmic variables (Nayakshin 2003). Its presence would nicely complement the low electron density (49) that we require within a hot RIAF in the FRB emission zone near the ISCO.

For example, the mid-plane of a thin gas pressure-dominated disk with opacity provided mainly by free-free absorption (Novikov & Thorne 1973) would reach the ionization threshold at an accretion rate

$$\frac{\dot M}{\dot M_{\rm edd}} = 0.005\,\alpha_{-2}^{2/3}\varepsilon_{{\rm rad},-1} M_{\bullet,6}^{2/3}\left(\frac{r}{10^4\,R_g}\right)^{5/2}. \tag{59}$$

A temporary shut off in torque at $\sim 10^4$ gravitational radii due to weak ionization would allow the inner parts of the disk to drain and also reach the ionization threshold, all the while remaining gravitationally stable.

As the disk at radius $D_{sm} \sim 10^2\,R_g$ drops to a mid-plane temperature of $\sim 10^4$ °K, its mid-plane scaleheight reaches

$$\frac{h}{D_{sm}} \sim 4\times 10^{-4}\,T_4^{1/2}\left(\frac{D_{sm}}{100\,R_g}\right)^{1/2}. \tag{60}$$

The vertically integrated mass column would drop to about $10^4\,M_{\bullet,6}^{4/5}$ g cm^{-2} for the normalizations of viscosity parameter α and inner radiation efficiency $\varepsilon_{\rm rad}$ given above. A thin, externally ionized surface layer of electron column $\sim 10^{20}$ cm^{-2} would sit at a height $z_{\rm ion} \sim 6\,h$ above the mid-plane, and have a scaleheight

$$\frac{h_{\rm ion}}{D_{sm}} \sim \frac{h^2}{z_{\rm ion} D_{sm}} \sim 6\times 10^{-5}\,T_4^{1/2}\left(\frac{D_{sm}}{100\,R_g}\right)^{1/2}. \tag{61}$$

The hydrostatic pressure in such a cool surface layer at the reflection density (56) is comparable to the external pressure of a RIAF with density $n_{e,\rm ISCO} \lesssim 10^7$ cm^{-3} at the ISCO and scaling as $n_e k_{\rm B} T_e \propto r^{-2}$ at larger radius. It is also straightforward to check that heating by Coulomb scattering warm electrons that penetrate the cool surface layer from the RIAF is not able to overcome in situ atomic cooling at a column $\gtrsim 10^{18}$ g cm^{-2}.

This quiescent surface scale height is marginally consistent with (58), suggesting that the duration of the reflected pulse will be determined by the geometric delay during reflection. In fact, the electron density in the ionized surface layer would reach the threshold for reflecting GHz waves at a column somewhat lower than the column that would be heated to relativistic energies by the highest-frequency part of the electromagnetic pulse. As a result, reflection of the GHz wave would occur at a depth in the mirror where the electrons were still mildly relativistic. The reflected wave frequency would be slightly modified by the bulk motion induced in the mirror electrons.

Additional sources of geometric delay come from the finite size of the emitting patch on the relativistic shell produced by the tiny FRB explosion. Consider the simplest case where the mirror does not magnify the electromagnetic pulse. Then the solid angle of the observable patch of the fireball surface is $\sim \pi/\Gamma_{\rm em}^2$, where $\Gamma_{\rm em}$ is the fireball Lorentz factor at the emission radius of the GHz photons. One finds $\Gamma_{\rm em} \sim 10^4$ from Equations (53) and (110) of Paper I. Two rays of the same frequency emitted from opposite sites of the observable patch experience a differential delay between emission and reflection

$$\Delta t_d \sim \frac{D_{sm}}{\Gamma_{\rm em}^2 c} \sim 3\times 10^{-6}\,\Gamma_{{\rm em},4}^{-2} D_{sm,13}\quad {\rm s}. \tag{62}$$

This would become observationally significant only if the plasma mirror magnified the GHz image, in which case Δt_d in Equation (62) would be increased by a factor m^2, where m is the magnification. Broadening could also arise from a high-wavenumber corrugation of the screen surface, through an angle $\delta\theta > \Gamma_{\rm em}^{-1}$.

8.4. *Cosmic Redshift Distribution of Electromagnetic Pulses*

Rare collisions between LSD particles in galactic halos are distributed broadly in cosmic redshift: we find a fairly uniform rate of 4×10^4 yr^{-1} per comoving Gpc^3 between $z=0$ and 2 for the LSD parameters of Figure 3 and 4 ($f_{\rm LSD}=1$ and $\mathcal{T}=10^{-8}c^4/G$).

On the other hand, collisions within LSD rings orbiting supermassive black holes are concentrated closer to the epoch when these black holes form by direct collapse of gas clouds (Section 6). This source of LSD collisions should be concentrated toward the redshift of peak SMBH assembly ($z\sim2$ as measured by bright AGN activity). Unfortunately a high annihilation rate driven by a high accretion rate onto a SMBH would also be accompanied by strong synchrotron absorption at GHz frequencies (Equation (49) and Paper I).

8.5. *Narrow and Ultra-Luminous 100 GHz Pulses from Nearby Supermassive Black Holes*

The collision of two LSDs of mass $\mathcal{M}\sim10^{20}$ g and size $\mathcal{R}\sim0.1$ cm releases $\sim10^{41}$ erg in electromagnetic energy and high-energy particles (in the case of 'spring' loops, this is if the currents have opposing signs). The high Lorentz factor achieved by this tiny explosion allows a high efficiency of conversion to photons of frequency $\nu_{\rm peak}\sim c/2\pi\mathcal{R}\sim50(\mathcal{R}_{-1})^{-1}$ GHz, decreasing as $\sim\nu^{0.5-1}$ toward lower frequencies (Paper I).

We have identified two channels for LSD collisions, identifying non-repeating FRBs with rare collisions in Galactic halos, whose rate is directly related to the the ratio $\mathcal{M}/\mathcal{R}$ (or equivalently to the string tension $\mathcal{T}$ in the 'spring' model). The collision rate near SMBHs involves a more complicated chain of events, but we expect it to be much larger.

Equation (39) shows that a SMBH could release O(1) electromagnetic burst each year even without the accretion of additional LSD. An even higher rate is possible if the SMBH experiences persistent accretion at a low rate. For example, if we restrict to black holes with masses less than or equal to the Galactic Center black hole ($\sim4\times10^6\,M_\odot$), then Equation (54) suggests that the rate per black hole is roughly $\sim10^2$ per year for a time-averaged accretion rate $\dot m\sim10^{-3}$. (This does not include an upward correction to the electromagnetic transient rate from gravitational lensing or reflection.) Taking a cosmic density of such SMBHs of 10^{-2} Mpc^{-3} (Caramete & Biermann 2010), we deduce a collision rate $\sim10^9$ Gpc^{-3} yr^{-1}, some $\sim10^4$-10^5 times the local non-repeating rate.

It should also be noted that a LSD cusp gathered around a SMBH would be disrupted by gravitational scattering if the SMBH experienced a merger with another black hole of high or intermediate mass. For this reason, FRBs may avoid the cores of massive elliptical galaxies. Although Equation (39) predicts a very high number of trapped LSDs around the most massive (10^8-$10^9\,M_\odot$) SMBHs, it is in such cases that the probability of a major merger appears to be highest (e.g. Faber et al. 1997).

With the preceding caveat in mind, we conclude that nearby $\sim10^{6-7}\,M_\odot$ SMBH are promising targets for directed searches for 0.01-1 THz bursts. These are predicted to be intrinsically brighter than GHz FRBs, and would more easily avoid absorption. We emphasize that most LSD collisions near SMBHs are not expected to be detectable sources of GHz pulses: even after accounting for the feedback of the strong wave on ambient electrons, the optical depth to synchrotron absorption remains high in the GHz band. This conclusion holds (although not by a large margin) for the Galactic Center SMBH, with its low present accretion rate (Yuan et al. 2012). (See Equation (49) and Paper I.) But the synchrotron optical depth is much smaller at 10-100 GHz.

We therefore highlight the prediction of a high rate of ~100 GHz bursts, mostly originating near SMBHs, which are similar to FRBs but an order of magnitude brighter. These pulses may be very narrow: as limited by multi-path propagation some $\sim10^{-4}$ times narrower than FRBs, corresponding to sub-microsecond durations.

8.6. *Direct Detection of μJy Radio Sources with Extreme Proper Motion*

The nearest LSD to the Earth is predicted to reside within our own Solar system: the mean separation between LSDs is $f_{\rm LSD}^{-1/3}(\rho_{\rm dm}/\mathcal{M})^{-1/3}\sim35\,f_{\rm LSD}^{-1/3}\mathcal{M}_{20}^{-1/3}$ AU, implying a mean distance $\sim20\,f_{\rm LSD}^{-1/3}\mathcal{M}_{20}^{-1/3}$ AU from the Sun. A LSD magnetosphere moving tangentially at a speed ~300 km s^{-1} through a solar wind of proton density ~0.02 cm^{-3} and radial speed 350 km s^{-1} would have a size $R_{\rm mag}\sim400\mathcal{M}_{20}^{1/6}\mathcal{R}_{-1}^{1/2}(a/20\ {\rm AU})^{1/3}$ km from Equation (12) and angular diameter less than 0.1 arcsec. Its lifetime at 20 AU from the Sun would would be ~0.3 yr, meaning that over a period of a few years the closest approach of a LSD to the Earth and Sun would be ~10 AU, with magnetopause radius shrinking by a factor $\sim2^{-1/3}$ and angular size increasing by a factor $\sim2^{2/3}$.

Consider then the observability of coherent decametric or radio emission from the LSD magnetosphere. In the absence of a predictive theory of such emission, we simply scale to planetary magnetospheres. For example, a fraction $\sim1\times10^{-4}$ of the Solar wind power incident on Jupiter's magnetosphere emerges as decametric emission, with much higher efficiencies in the infrared band (Bhardwaj & Gladstone 2000). The Solar wind power incident on an LSD magnetosphere would be

$$\begin{aligned}\mathcal{P}_w&\sim\frac{1}{2}\rho_wV_w^3\cdot\pi R_{\rm mag}^2\\&=3\times10^{12}\,\mathcal{M}_{20}^{1/3}\mathcal{R}_{-1}^{2/3}(a/20\ {\rm AU})^{-4/3}\quad{\rm erg\ s^{-1}}.\end{aligned}\tag{63}$$

The emission efficiency needed to produce a μJy source in the GHz band at this distance from the Earth is

$$f_{\rm GHz}\sim3.5\times10^{-3}\,\mathcal{M}_{20}^{-1/3}\mathcal{R}_{-1}^{-2/3}\nu_9(a/20\ {\rm AU})^{10/3}.\tag{64}$$

Picking out a single sub-arcsecond source of this low luminosity and enormous proper motion from the entire sky would certainly be challenging; but it would represent a direct detection of macroscopic dark matter and support for the ideas presented here.

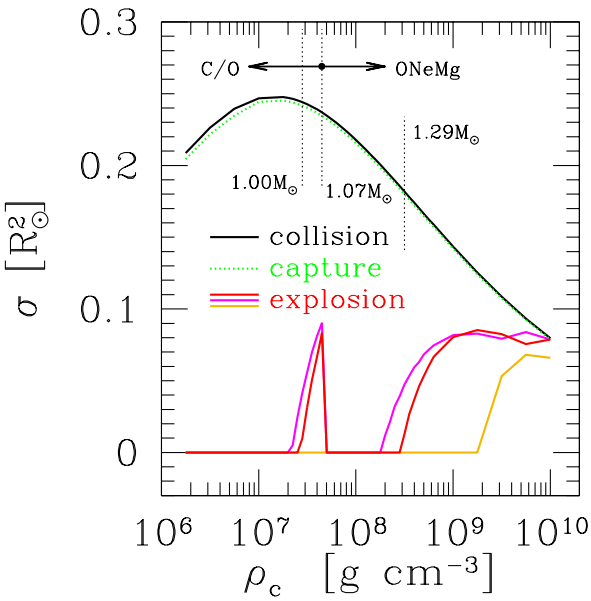

FIG. 14.— Cross section for a LSD of tension $\mathcal{T} = 10^{-8}c^4/G$ and mass $\mathcal{M} = 4\times10^{20}$ g, moving at 200 km s^{-1} at infinity, to interact with a WD of varying mass and central density. *Solid black curve:* collision. *Dotted green curve:* collision and frictional trapping. *Red curve:* strong enough heating to trigger a deflagration/detonation, corresponding to $t_{\rm ign} < R_{\rm mag}/V_{\rm ps}$. *Magenta curve:* same as red curve, but for LSD of mass $\mathcal{M} = 4\times10^{19}$. *Gold curve:* same as red curve, but for LSD of tension $G\mathcal{T}/c^4 = 10^{-9}$ and mass $\mathcal{M} = 4\times10^{19}$ g (corresponding to an identical dipole size).

8.7. *Constraints from Sub-Pixel Microlensing*

Microlensing of stars in M31 strongly constrains the abundance of dark matter particles of masses exceeding $\sim 10^{20}$-10^{21} g (Niikura et al. 2017) The lensing is detected below the pixel angular scale of a CCD detector (Crotts 1992), and the precise value of the mass threshold depends on details like the finite size of the lensed stars. Comparing with Equation (33) for the radiated energy in GHz photons, one sees that this mass constraint is consistent with a 'spring' tension $\mathcal{T} \sim 10^{-8}c^4/G$ (the value that is needed to give a collision rate comparable to the observed FRB burst rate) and a conversion efficiency $f_{\rm em} \sim 1$ of the mass of two colliding springs to the broadband electromagnetic pulse.

Collisional LSDs that are trapped near SMBH can combine to form a higher-energy tail that can easily extend one-two orders of magnitude higher than the rest energy of the seed LSD (Figure 7). If such a collisional population of LSDs were to dominate the observed FRB rate, then the mass limit from microlensing could be easily avoided for a larger tension $G\mathcal{T}/c^4 \sim 10^{-7}$. In the approach to FRBs advanced here, this would be the case for the repeating source FRB 121102.

Future microlensing searches will provide tight constraints on LSD progenitors of FRBs given the small difference between the microlensing mass constraint and the minimum LSD mass needed to power GHz FRB emission.

8.8. *Induced Thermonuclear Explosions of Massive ($> 1\,M_\odot$) White Dwarf Stars*

The interaction between LSDs and WD stars has observational consequences, involving i) the triggering of hydrogen-depleted (Type Ia) supernova explosions; ii) the enrichment of galactic and intergalactic plasma with iron group elements; and iii) the depletion of the massive tail of the WD population. We now consider these effects in turn.

We found a threshold WD mass ($M_{\rm wd} = 1.0\,M_\odot$ for C/O and $1.29\,M_\odot$ for ONeMg composition) above which self-sustained thermonuclear burning would be triggered by the infall of a LSD of tension $\mathcal{T} = 10^{-8}c^4/G$ (Figure 10). The corresponding interaction cross section is compared in Figure 14 with the total cross section for a direct collision. Reducing the LSD mass from 4×10^{20} g to 4×10^{19} g, and the radius in proportion to the mass (corresponding to a fixed 'spring' tension), slightly increases the drag time (15), and therefore the post-shock temperature during the deceleration of the LSD. As a result, explosions are slightly easier and the susceptible range of WD masses widened slightly. On the other hand, reducing the mass by the same amount but fixing the LSD radius significantly reduces the drag time, and makes it harder to reach high temperatures. In this case, only the most massive ONeMg WDs develop self-sustained burning.

Recall also that burning is triggered relatively deeply in the C/O material (typically an enclosed mass below $\sim \frac{1}{2}M_{\rm wd}$), but in relatively shallow layers of the more massive WDs (Figure 12). This feature of the trigger mechanism is increasingly testable by measurements of the early light curves of nearby Type Ia explosions, which probe the ^{56}Ni yield in the outer ejecta shells (e.g. SN 2011fe: Piro 2012).

Combined nucleosynthetic and radiation transfer calculations of the detonations of $\sim 1\,M_\odot$ C/O WDs give encouraging light curves (Sim et al. 2010) while avoiding the complications associated with a deflagration-to-detonation transition. Nonetheless, as we discussed in Section 7.4, the shock induced by a LSD moving through a WD appears to be a couple orders of magnitude too small to produce an unambiguous prompt detonation. The extent to which this conclusion depends on the extended (linear) geometry of the energy release needs further examination.

8.8.1. *Lifetime of Local Massive White Dwarfs*

Consider first the lifetime for a WD in the quoted range of masses. Figure 14 shows the cross section to induce a thermonuclear explosion,

$$\sigma_{\rm exp} = \frac{\pi\ell_{\rm exp}^2}{(\Delta v)^2}. \tag{65}$$

Here $\ell_{\rm exp}$ is the corresponding angular momentum of the LSD particle, with respect to the target WD. In the case of $1.0 - 1.07\,M_\odot$ C/O WDs, we find that $\sigma_{\rm exp}$ averages to about $\sim 1/6$ the collision cross section $\sigma_{\rm col} = \pi\ell_{\rm col}^2/(\Delta v)^2$.

A target WD is assumed to reside in a rotating galactic disk that is immersed in a non-rotating and locally isothermal dark matter halo with LSD mass fraction $f_{\rm LSD}$. The distribution function of halo particles,

$f(\mathbf{v}) \propto e^{-v^2/2\sigma^2}$, has a dispersion related to the circular speed by

$$\sigma_{\rm LSD} = V_c/\sqrt{2}. \quad (66)$$

Averaging over the LSD velocity space $\mathbf{v}$, with $\Delta v = \sqrt{v_x^2 + v_y^2 + (v_z - V_c)^2}$, gives

$$\langle \Delta v \sigma_{\rm exp} \rangle = \pi \ell_{\rm exp}^2 \left\langle \frac{1}{\Delta v} \right\rangle = \frac{\pi \ell_{\rm exp}^2}{V_c} \, {\rm erf}\left(\frac{V_c}{\sqrt{2}\sigma} \right). \quad (67)$$

Here ${\rm erf}(1) = 0.843$.

We obtain a mean lifetime for a nearby $1\,M_\odot$ WD to survive a collision with a LSD particle,

$$t_{\rm col}(1\,M_\odot) = \frac{\mathcal{M}}{f_{\rm LSD}\rho_{\rm dm}\langle \Delta v \sigma_{\rm exp}\rangle} = 1.8 \times 10^9 \, f_{\rm LSD}^{-1} \mathcal{M}_{20} \left(\frac{\sigma_{\rm col}/6}{\sigma_{\rm exp}} \right) \quad {\rm yr}. \quad (68)$$

The lifetime of massive ONeMg WDs is roughly half this (Figure 14). Here we have used values for the local Milky Way dark matter density, $\rho_{\rm dm} \simeq 7 \times 10^{-25}$ g cm^{-3}, and circular speed $V_c = 230$ km s^{-1}, taken from McMillan (2017).

If LSDs comprise a large fraction of the Galactic dark matter, collisions with them produce a strong depletion of nearby cold and massive WDs in the mass intervals $1.0 - 1.07\,M_\odot$ and $> 1.29\,M_\odot$. This mass function is not yet accurately measured, but it provides strong potential tests of the mechanism of WD disruption described here. Evidence for a depletion of massive WDs closer than 20 pc to the Sun has been discussed by Tremblay et al. (2016), whereas evidence for a feature near $1\,M_\odot$ in the mass spectrum of local WDs cooler than 12,000 °K has been described by Rebassa-Mansergas et al. (2015).

The lifetime of a massive WD will depend on its position within its host galaxy, decreasing toward the center. Massive white dwarfs also appear to survive in binary systems, but estimates of their ages are made ambiguous by the possibility of mass growth by accretion, and so we do not consider the constraints imposed by their existence here.

8.8.2. *Global Rate of LSD-Induced WD Explosions*

If the LSD mass is in the range ($\mathcal{M} \sim 10^{20}$ g) we find is necessary to power FRBs of energy 10^{39} erg, WDs in quoted mass range will have lifetimes significantly shorter than the age of the universe: a large fraction are eventually destroyed by collision with a LSD.

This leads to a well defined prediction for the number of Type Ia supernovae per unit stellar mass, averaged over cosmic volume. We take a Kroupa (2001) stellar initial mass function (IMF) $dN/dM_\star$,

$$\frac{dN}{dM_\star} = \begin{cases} (K_1/M_{\star 1})(M_\star/M_{\star 1})^{-\alpha_1} & (M_\star < M_{\star 1}) \\ (K_1/M_{\star 1})(M_\star/M_{\star 1})^{-\alpha_2} & (M_{\star 1} < M_\star < M_{\star 2}) \\ (K_3/M_{\star 2})(M_\star/M_{\star 2})^{-\alpha_3} & (M_\star > M_{\star 2}) \end{cases} \quad (69)$$

Here $M_{\star 1} = 0.08\,M_\odot$, $M_{\star 2} = 0.5\,M_\odot$, $\alpha_1 = 0.3$, $\alpha_2 = 1.7$ and $\alpha_3 = 2.3$. The coefficients K_i are related to the total stellar mass by $K_1 = 0.77\,M_{\star,\rm tot}/M_\odot = 1.73 K_3$.

To obtain an explosion rate, we make use of the relation between zero-age main sequence stellar mass and WD mass obtained from state-of-the-art stellar evolution calculations (Doherty et al. 2015). All numbers quoted here refer to solar metallicity. A star of mass $M_\star > M_{\star,1} = 5.8\,M_\odot$ is needed to produce a $1\,M_\odot$ WD, increasing to $M_{\star,2} = 6.4\,M_\odot$ for the highest mass C/O WDs ($1.07\,M_\odot$). We neglect the possibility of hybrid carbon-ONeMg WDs here. Finally ONeMg WDs with mass exceeding $1.29\,M_\odot$ form from $7.9 - 8.5\,M_\odot$ progenitors. Integrating over the initial progenitor mass for C/O WDs heavier than $1\,M_\odot$, we find

$$N_{\rm Ia}({\rm C/O}) = \int_{M_{\star,1}}^{M_{\star,2}} dM_\star \frac{dN}{dM_\star} = 1.7 \times 10^{-3} \frac{M_{\star,\rm tot}}{M_\odot}. \quad (70)$$

The corresponding yield of ONeMg WDs more massive than $1.29\,M_\odot$ is

$$N_{\rm Ia}({\rm ONeMg}) = 8.5 \times 10^{-4} \frac{M_{\star,\rm tot}}{M_\odot}. \quad (71)$$

Deductions of the Type Ia SN rate from measurements of iron enrichment in the hot plasma of rich galaxy clusters suggests a normalization $N_{\rm Ia} \simeq 3.4 \times 10^{-3}\,M_{\star,\rm tot}/M_\odot$, based on a ^{56}Fe yield of $0.7\,M_\odot$ per explosion; whereas the observed rates of Type Ia supernova in galaxy clusters suggest values $\sim 2 - 2.5 \times 10^{-3}\,M_{\star,\rm tot}/M_\odot$ (Maoz & Mannucci 2012).

The approximate agreement of Equations (70) and (71) with these empirical values is encouraging: our evaluation of the Type Ia rate depends only a i) a prescribed WD mass range within which LSD collisions produce explosions and ii) the stellar IMF. Furthermore, this triggering mechanism is agnostic as to the situation of the target WD, which could be a single star as well one accompanied by a degenerate or non-degenerate companion. Type Ia supernovae are predicted to arise from all types of WD binaries with a frequency proportional to their formation rate, at least to the extent that these rates do not depend on the local stellar or dark matter density.

8.9. *Constraints on 'Spring' Tension from CMB Lensing and Low-Frequency Gravity Wave Emission*

The concrete microphysical example of LSDs given here involves macroscopic loops of GUT-scale superconducting strings. The spread in loop masses is restricted to lie within a decade centered around the value ($\mathcal{M} \sim 10^{20}$ g) needed to power FRBs. If loops a decade or two smaller made a significant contribution to the cold dark matter density, then WDs with masses exceeding $\sim 1\,M_\odot$ would have a lifetime shorter than $\sim 10^7$-10^8 yrs. A significant density in loops with masses exceeding $\sim 10^{21}$ g appears to be inconsistent with the absence of short-timescale microlensing of stars in M31 (Niikura et al. 2017).

At first sight, such a peaked distribution of loop sizes is not consistent with the approach to cosmic string formation initiated by Kibble (1976). This involves an infinite network of string combined with closed loops that break off the string during its self-intersection. This network has no characteristic scale smaller than the comoving

horizon size during the symmetry breaking phase transition that created the string network. In Section 8.10 we make a connection between $\sim$ mm-sized LSDs and low-temperature post-inflationary preheating of the universe.

The long string which might be present plays no role in the FRB emission process described here and in Paper I, but would have observational consequences involving i) gravity wave emission (Vilenkin 1981; Turok 1984; Vachaspati & Vilenkin 1985); ii) gravitational lensing of background galaxies (Vilenkin 1984; Kaiser & Stebbins 1984; Gott 1985); and gravitational lensing of the cosmic microwave background (CMB) (Planck Collaboration et al. 2014; Lazanu et al. 2015; Lizarraga et al. 2016). Kink-like structure on the string and loops with redshifted periods of $P_{\rm gw} \sim 1$ year have a size limited by gravity-wave emission. The emission redshift is determined from

$$\frac{G\mathcal{T}}{c^4} ct(z_{\rm em}) \sim \frac{cP_{\rm gw}}{1+z_{\rm em}} \tag{72}$$

and is relatively small, $1 + z_{\rm em} \sim 10^4\,(G\mathcal{T}/c^4)_{-8}$.

As a result, any long-string network associated with the LSD loops should lens the CMB and produce gravitational radiation in the standard amount. An upper bound $G\mathcal{T}/c^4 < 1.3\times10^{-7}$ has been derived by combining data from the Planck satellite and from the high-ℓ microwave background experiments ACT and SPT (Planck Collaboration et al. 2014). A nearly identical constraint is derived by combining these data with string network simulations (Lazanu et al. 2015; Lizarraga et al. 2016). The most conservative current bounds from pulsar timing are $G\mathcal{T}/c^4 \lesssim 1.3\times10^{-7}$ from the EPTA (Lentati et al. 2015) and $G\mathcal{T}/c^4 < 3.3\times10^{-8}$ from the NANOGrav experiment (Arzoumanian et al. 2016). These constraints allow the size of string loops to be freely variable; a much tighter constraint, $G\mathcal{T}/c^4 < 1.3\times10^{-10}$ (Arzoumanian et al. 2016), is derived from a more conventional estimate of loop size as determined by self-intersection and decay by the emission of gravitational waves. The CMB constraints and most conservative versions of the pulsar timing constraints are therefore consistent with a 'spring' tension $\mathcal{T} \sim 10^{-8}c^4/G$, but it is apparent that significant departures from the standard string network calculations must be present to accomodate more fully the pulsar timing results.

Finally, we note that strong gravitational lensing by the long string would occur on a scale $8\pi G\mathcal{T}/c^4 = 0.05(G\mathcal{T}/c^4)_{-8}$ arcsec. This angular scale is small enough to have been missed so far by observational searches for strong lenses.

8.10. *Formation During Post-Inflationary Preheating*

When considering the origin of macroscopic field structures in the early universe, two useful reference points are i) the mass-energy contained with a horizon-sized volume at the epoch of their formation; and ii) the mass of dark matter extrapolated backward in the cosmic expansion to this volume. Our focus here is on the electroweak scale. The temperature of electroweak symmetry restoration implied by a minimal standard model Higgs particle of mass 125 GeV is $k_{\rm B}T_{\rm EW} \simeq 165$ GeV (Dine et al. 1992), at a redshift $z_{\rm EW} = (T_{\rm EW}/T_{\rm CMB})\times[g_{*,\rm EW}/3]^{1/3} = 2.3\times10^{15}$, where $g_{*,\rm EW} \simeq 107$ is the number of relativistic degrees of freedom at this temperature. One finds

$$M_{\rm hor}(z) = \left(\frac{c}{H}\right)^3 \frac{\pi^2 g_*}{30\hbar^3c^5}(k_{\rm B}T)^4 \sim 10^{27}\left(\frac{z}{z_{\rm EW}}\right)^{-2}\ {\rm g}, \tag{73}$$

where H is the Hubble parameter at redshift $z < z_{\rm EW}$. By comparison, the cold dark matter mass is

$$M_{\rm d,H}(z) = \left(\frac{c}{H}\right)^3 (1+z)^3\rho_d(0) \sim 5\times10^{15}\left(\frac{z}{z_{\rm EW}}\right)^{-3}\ {\rm g}. \tag{74}$$

The LSD mass $\mathcal{M} \sim 10^{20}$ g considered here is intermediate between these two values. That means that Friedmann-type expansion through the electroweak phase transition can only produce stable macroscopic field structures of a much smaller mass. On the other hand, higher LSD masses are possible if the entropy/dark matter ratio increases with time, which would be the case if inflationary preheating occurred at a temperature below $T_{\rm EW}$. Equating expression (74) with $\mathcal{M}$ gives a preheating temperature $T_{\rm pr} \sim 0.03\,T_{\rm EW}$.

APPENDIX

COLLISIONAL CROSS SECTION OF FREE CLASSICAL DIPOLES

The equations describing the collision between two dipoles ($i, j = 1, 2$ and $i \neq j$) are

$$\begin{aligned}
\mathcal{M}_r\frac{d\mathbf{v}_{ij}}{dt} &= \frac{\partial[\boldsymbol{\mu}_i\cdot\mathbf{B}_j(\mathbf{r}_{ij})]}{\partial\mathbf{r}_i} = -\frac{\partial[\boldsymbol{\mu}_j\cdot\mathbf{B}_i(\mathbf{r}_{ij})]}{\partial\mathbf{r}_j};\\
\frac{d\boldsymbol{\mu}_i}{dt} &= \boldsymbol{\Omega}_i\times\boldsymbol{\mu}_i;\\
\mathcal{I}_i\frac{d\boldsymbol{\Omega}_i}{dt} &= \boldsymbol{\mu}_i\times\mathbf{B}_j(\mathbf{r}_{ij});\quad \boldsymbol{\Omega}_i\cdot\mathbf{B}_j(\mathbf{r}_{ij}) = {\rm const};\\
\mathbf{r}_{ij} &= r_{ij}\hat{r}_{ij} = \mathbf{r}_i - \mathbf{r}_j;\quad \mathbf{v}_{ij} = \frac{d\mathbf{r}_{ij}}{dt}.
\end{aligned} \tag{A1}$$

Here $\mathcal{M}_r = \mathcal{M}_1\mathcal{M}_2/(\mathcal{M}_1+\mathcal{M}_2)$ is the reduced mass, $\mathbf{B}_i$ is the magnetic field sourced by dipole i, and

$$-\boldsymbol{\mu}_1\cdot\mathbf{B}_2(\mathbf{r}_{12}) = -\boldsymbol{\mu}_2\cdot\mathbf{B}_1(\mathbf{r}_{21}) = \frac{\boldsymbol{\mu}_1\cdot\boldsymbol{\mu}_2 - 3(\boldsymbol{\mu}_1\cdot\hat{r}_{12})(\boldsymbol{\mu}_2\cdot\hat{r}_{12})}{r_{12}^3} \tag{A2}$$

is the interaction energy. Scaling distances to $R_{\rm col} = (2\mu_1\mu_2/\mathcal{M}_r(\Delta v)^2)^{1/3}$, and the time to $R_{\rm col}/\Delta v$, one finds

$$\frac{R_{\rm col}}{\Delta v^2}\frac{d\mathbf{v}_{ij}}{dt} = \frac{3}{2}\left(\frac{R_{\rm col}}{r_{12}}\right)^4 \left[\hat{\mu}_i(\hat{\mu}_j\cdot\hat{r}_{ij}) + \hat{\mu}_j(\hat{\mu}_i\cdot\hat{r}_{ij}) + \hat{r}_{ij}(\hat{\mu}_i\cdot\hat{\mu}_j - 5\hat{\mu}_i\cdot\hat{r}_{ij}\hat{\mu}_j\cdot\hat{r}_{ij})\right]. \tag{A3}$$

We also scale the two rotational moments of inertia to a characteristic value, $\mathcal{I}_i = \widetilde{\mathcal{I}}_i\mathcal{I}$, and the angular velocity to $\mathbf{\Omega}_i = (\Delta v/R_{\rm col})\, f\, \hat{\Omega}_i$, where $f = (\mathcal{M}_r R_{\rm col}^2/2\mathcal{I})^{1/2}$ is the fastness parameter. This gives

$$\begin{aligned} \frac{R_{\rm col}}{\Delta v}\frac{d\hat{\mu}_i}{dt} &= f\left(\hat{\Omega}_i\times\hat{\mu}_i\right); \\ \widetilde{\mathcal{I}}_i\frac{R_{\rm col}}{\Delta v}\frac{d\hat{\Omega}_i}{dt} &= f\left(\frac{R_{\rm col}}{r_{12}}\right)^3 \hat{\mu}_i\times\left[3(\hat{\mu}_j\cdot\hat{r}_{ij})\hat{r}_{ij} - \hat{\mu}_j\right]. \end{aligned} \tag{A4}$$

The Equations (A3), (A4) are solved for a large number of randomly chosen initial orientations of the two colliding dipoles to obtain the cross section shown in Figure 2.

REFERENCES

Arzoumanian, Z., Brazier, A., Burke-Spolaor, S., et al. 2016, ApJ, 821, 13
Bailey, A. B., & Hiatt, J. 1972, AIAA Journal, 10, 1436
Begelman, M. C., Volonteri, M., & Rees, M. J. 2006, MNRAS, 370, 289
Bhardwaj, A., & Gladstone, G. R. 2000, Reviews of Geophysics, 38, 295
Binney, J., & Tremaine, S. 2008, Galactic Dynamics: Second Edition, Princeton University Press, Princeton
Blandford, R. D. 1977, MNRAS, 181, 489
Blandford, R. D., & Begelman, M. C. 1999, MNRAS, 303, L1
Capela, F., Pshirkov, M., & Tinyakov, P. 2013, Phys. Rev. D, 87, 023507
Capela, F., Pshirkov, M., & Tinyakov, P. 2014, Phys. Rev. D, 90, 083507
Caramete, L. I., & Biermann, P. L. 2010, A&A, 521, A55
Caughlan, G. R., & Fowler, W. A. 1988, Atomic Data and Nuclear Data Tables, 40, 283
Chatterjee, S., Law, C. J., Wharton, R. S., et al. 2017, Nature, 541, 58
Choi, J.-H., Shlosman, I., & Begelman, M. C. 2013, ApJ, 774, 149
Choi, J.-H., Shlosman, I., & Begelman, M. C. 2015, MNRAS, 450, 4411
Churazov, E., Khabibullin, I., Sunyaev, R., & Ponti, G. 2017, MNRAS, 465, 45
Copeland, E., Turok, N., & Hindmarsh, M. 1987, Physical Review Letters, 58, 1910
Crawford, F., Rane, A., Tran, L., et al. 2016, MNRAS, 460, 3370
Crotts, A. P. S. 1992, ApJ, 399, L43
Davis, R. L., & Shellard, E. P. S. 1989, Nuclear Physics B, 323, 209
Dine, M., Leigh, R. G., Huet, P., Linde, A., & Linde, D. 1992, Phys. Rev. D, 46, 550
Doherty, C. L., Gil-Pons, P., Siess, L., Lattanzio, J. C., and Lau, H. H. B. 2015, MNRAS, 446, 2599
Dursi, L. J., & Timmes, F. X. 2006, ApJ, 641, 1071
Faber, S. M., Tremaine, S., Ajhar, E. A., et al. 1997, AJ, 114, 1771
Farmer, R., Fields, C. E., & Timmes, F. X. 2015, ApJ, 807, 184
Fattahi, A., Navarro, J. F., Sawala, T., et al. 2016, arXiv:1607.06479
Gondolo, P., & Silk, J. 1999, Physical Review Letters, 83, 1719
Gott, J. R., III 1985, ApJ, 288, 422
Governato, F., Zolotov, A., Pontzen, A., et al. 2012, MNRAS, 422, 1231
Graham, P. W., Rajendran, S., & Varela, J. 2015, Phys. Rev. D, 92, 063007
Gültekin, K., Richstone, D. O., Gebhardt, K., et al. 2009, ApJ, 698, 198
Haws, D., Hindmarsh, M., & Turok, N. 1988, Physics Letters B, 209, 255
Kaiser, N., & Stebbins, A. 1984, Nature, 310, 391
Katz, J. I. 2016, arXiv:1611.01243
Kibble, T. W. B. 1976, Journal of Physics A Mathematical General, 9, 1387
Klypin, A. A., Trujillo-Gomez, S., & Primack, J. 2011, ApJ, 740, 102
Kroupa, P. 2001, MNRAS, 322, 231
Lazanu, A., Shellard, E. P. S., & Landriau, M. 2015, Phys. Rev. D, 91, 083519
Lentati, L., Taylor, S. R., Mingarelli, C. M. F., et al. 2015, MNRAS, 453, 2576
Lizarraga, J., Urrestilla, J., Daverio, D., Hindmarsh, M., & Kunz, M. 2016, Journal of Cosmology and Astroparticle Phys., 10, 042
Loeb, A., & Rasio, F. A. 1994, ApJ, 432, 52
Lorimer, D. R., Bailes, M., McLaughlin, M. A., Narkevic, D. J., & Crawford, F. 2007, Science, 318, 777
Luan, J., & Goldreich, P. 2014, ApJ, 785, L26
Maoz, D., & Mannucci, F. 2012, P.A.S.A., 29, 447
Marcote, B., Paragi, Z., Hessels, J. W. T., et al. 2017, ApJ, 834, L8
McMillan, P. J. 2017, MNRAS, 465, 76
Nayakshin, S. 2003, Astronomische Nachrichten Supplement, 324, 483
Navarro, J. F., Frenk, C. S., & White, S. D. M. 1997, ApJ, 490, 493
Niemeyer, J. C., & Woosley, S. E. 1997, ApJ, 475, 740
Niikura, H., Takada, M., Yasuda, N., et al. 2017, arXiv:1701.02151
Novikov, I. D., & Thorne, K. S. 1973, in Black Holes, eds. C. DeWitt and B. DeWitt (Paris: Gordon and Breach), pp. 343-450
Ostriker, J. P., Thompson, C., & Witten, E. 1986, Physics Letters B, 180, 231
Peebles, P. J. E. 1972, General Relativity and Gravitation, 3, 63
Piro, A. L. 2012, ApJ, 759, 83
Planck Collaboration, Ade, P. A. R., Aghanim, N., etal. 2014, A&A, 571, A25
Planck Collaboration, Ade, P. A. R., Aghanim, N., etal. 2016, A&A, 594, A13
Prada, F., Klypin, A. A., Cuesta, A. J., Betancort-Rijo, J. E., & Primack, J. 2012, MNRAS, 423, 3018
Ravi, V., Shannon, R. M., Bailes, M., et al. 2016, Science, 354, 1249
Rebassa-Mansergas, A., Rybicka, M., Liu, X.-W., Han, Z., & García-Berro, E. 2015, MNRAS, 452, 1637
Schaller, M., Frenk, C. S., Theuns, T., et al. 2016, MNRAS, 455, 4442
Scholz, P., Spitler, L. G., Hessels, J. W. T., et al. 2016, ApJ, 833, 177
Shakura, N. I., & Sunyaev, R. A. 1973, A&A, 24, 337
Sim, S. A., Röpke, F. K., Hillebrandt, W., et al. 2010, ApJ, 714, L52
Spitler, L. G., Scholz, P., Hessels, J. W. T., et al. 2016, Nature, 531, 202
Steigman, G., Sarazin, C. L., Quintana, H., & Faulkner, J. 1978, AJ, 83, 1050
Tendulkar, S. P., Bassa, C. G., Cordes, J. M., et al. 2017, ApJ, 834, L7
Thornton, D., Stappers, B., Bailes, M., et al. 2013, Science, 341, 53

Thompson, C. ApJ, submitted, arXiv:1703.00393
Timmes, F. X., & Swesty, F. D. 2000, ApJS, 126, 501
Tremblay, P.-E., Cummings, J., Kalirai, J. S., et al. 2016, MNRAS, 461, 2100
Turok, N. 1984, Nuclear Physics B, 242, 520
Vachaspati, T., & Vilenkin, A. 1985, Phys. Rev. D, 31, 3052
Vilenkin, A. 1981, Physics Letters B, 107, 47
Vilenkin, A. 1984, ApJ, 282, L51
Wang, J., & Merritt, D. 2004, ApJ, 600, 149
Witten, E. 1985, Nuclear Physics B, 249, 557
Young, P. 1980, ApJ, 242, 1232
Yu, Y.-W., Cheng, K.-S., Shiu, G., & Tye, H. 2014, J. Cosmol. Astropart. Phys., 11, 040
Yuan, F., Quataert, E., & Narayan, R. 2003, ApJ, 598, 301
Yuan, F., Wu, M., & Bu, D. 2012, ApJ, 761, 129